doi:10.26443/seismica.v2i4.1540

Possible Shallow Tectonic Tremor Signals Near the Deformation Front in Central Cascadia

Zoe Krauss *[1], **William S.D. Wilcock** [2], **Kenneth C. Creager** [1]

[1]Department of Earth and Space Sciences, University of Washington, Seattle, [2]School of Oceanography, University of Washington, Seattle, WA

Author contributions: *Conceptualization*: Z. Krauss, W. S.D. Wilcock, K. Creager. *Data Curation*: Z. Krauss. *Formal Analysis*: Z. Krauss. *Funding Acquisition*: Z. Krauss, W. S.D. Wilcock. *Investigation*: Z. Krauss. *Methodology*: Z. Krauss, W. S.D. Wilcock, K. Creager. *Project Administration*: Z. Krauss, W. S.D. Wilcock. *Resources*: W. S.D. Wilcock. *Software*: Z. Krauss. *Supervision*: W. S.D. Wilcock, K. Creager. *Validation*: Z. Krauss. *Visualization*: Z. Krauss. *Writing – original draft*: Z. Krauss. *Writing – review & editing*: Z. Krauss, W. S.D. Wilcock, K. Creager.

Abstract To better constrain the locking state of the shallow Cascadia megathrust, we investigate whether shallow tectonic tremor occurs near the deformation front at ~44.5°N during 2015-2024. We focus on two cabled buried ocean bottom seismometers (OBSs) on the portion of Cascadia that has evidence of partial locking offshore: one at Slope Base on the incoming plate ~5 km from the deformation front, and another ~20 km east on the overriding plate at Southern Hydrate Ridge. We first use in situ measured bottom currents to show that shallow burial successfully prevents current-generated noise on OBSs. We then develop a single-station approach to isolate tectonic tremor-like signals based on waveform and spectral characteristics. This technique allows the use of isolated stations and small networks and accounts for emergent signals specific to the marine environment, namely T-phases and ship noise. Application of this approach to the buried OBSs in central Cascadia detects tectonic tremor-like signals at the Slope Base site only that cannot easily be attributed to instrumental or environmental noise. Additional observations are required to verify the origin of these signals, but possible sources include localized slow slip on the décollement, protothrusts, faults on the incoming plate, nearby strike-slip faults, or deformation within the outermost accretionary wedge.

Production Editor: Christie Rowe
Handling Editor: Alice Gabriel
Copy & Layout Editor: Anna Ledeczi

Signed reviewer(s): Anne Tréhu

Received: 20 December 2024
Accepted: 25 July 2025
Published: 19 August 2025

1 Introduction

Subduction zones host the largest faults on the planet and have the potential to generate devastating M9 megathrust earthquakes and tsunamis. Geophysical observations over the past several decades have shown that slip on these faults can occur not only as earthquakes, but also as slow slip events, where stable slip can last from hours to weeks (Beroza and Ide, 2011; Bürgmann, 2018; Peng and Gomberg, 2010; Rubinstein et al., 2009b). Stable slow slip can accommodate a significant portion of overall plate motion and reduce the amount of slip in megathrust events (e.g., Ramos et al., 2021). Slow slip events have also been identified as potential precursors to megathrust earthquakes (e.g., Kato et al., 2012; Meng et al., 2015). Constraints on whether a subduction zone is completely locked, or undergoes interseismic slow slip, has great bearing on anticipated coseismic and tsunamigenic hazard (Borghi et al., 2016; Carvajal et al., 2022). However, for subduction zones, much of the region of potential stable slow slip lies offshore, where geophysical observations are limited. Improving the ability to make seafloor observations of slow slip is therefore important for constraining subduction zone locking and megathrust hazard.

Tectonic tremor, a non-impulsive seismic signal at 1-10 Hz, is an indicator of slow slip and its presence can inform plate locking state (Ide et al., 2007). Across the global subduction zone network, tectonic tremor has been shown to accompany slow slip at shallow depths above the locked zone, in Japan (Annoura et al., 2017; Obana and Kodaira, 2009; Yamashita et al., 2015), Chile (Sáez et al., 2019), New Zealand (Todd et al., 2018), Costa Rica (Walter et al., 2011, 2013) and Central America (Plata-Martinez et al., 2021). However, in contrast to tectonic tremor observed at deeper depths below the locked zone, which displays a broad distribution over hundreds of kilometers (e.g., Ide, 2012; Wech, 2021), shallow tectonic tremor tends to be patchy and more limited along-strike (< ~100 km maximum patch width, e.g. Takemura et al. 2023). Shallow tectonic tremor also tends to be concentrated around subducting features including seamounts and ridges (Ogiso and Tamaribuchi, 2022; Todd et al., 2018; Plata-Martinez et al., 2021; Sáez et al., 2019).

Tectonic tremor is traditionally detected using the network-based method of envelope cross-correlation, which identifies a coherent emergent signal across several seismometers and localizes the signal source in space (Obara, 2002; Wech and Creager, 2008). This technique has been successful in identifying shallow tectonic tremor in offshore areas where station spacing is small (< ~25 km) and the instruments are relatively close to the tremor source (< ~40 km) (Annoura et al., 2017; Obana and Kodaira, 2009; Todd et al., 2018; Plata-Martinez et al., 2021; Sáez et al., 2019). However, autonomous ocean bottom seismometer (OBS) experiments that prioritize covering large areas, such as

*Corresponding author: zkrauss@uw.edu

the Cascadia Initiative and Alaska Amphibious Community Seismic Experiment (Barcheck et al., 2020; Toomey et al., 2014), are not well suited for envelope cross-correlation because their station spacing often exceeds ~50 km. Alternatively, single-station methods have been explored to identify periods of tectonic tremor based on long-duration dominance of the tremor frequency band (~1-10 Hz) over earthquake- or anthropogenic noise-dominated frequency bands (Brudzinski and Allen, 2007; Sit et al., 2012). These single-station methods have proven effective in detecting deep tremor on land-based stations, where tremor tends to last for days at a time, but may not work as well for detecting offshore shallow tremor, which tends to be patchier and shorter in duration (e.g., Takemura et al., 2023).

The identification of tectonic tremor on OBSs is further complicated by marine-specific emergent signals in the same 1-10 Hz frequency band (Wilcock et al., 2014). These include noise from passing ships (e.g., Ross and Kuperman, 1989) and T-phases (e.g., De Caro et al., 2020), which are tertiary earthquake arrivals that travel in the water column. T-phases are typically spindle-shaped (Talandier and Okal, 2001) and can be attenuated at higher frequencies, such that they can be picked in the same 1-10 Hz band as tectonic tremor (Hanson and Bowman, 2006; Lawrence, 2004). T-phases can be distinguished from tectonic tremor because they are better recorded on hydrophones, but they can cause tectonic tremor misdetections on OBSs when using the envelope cross-correlation method (Tréhu et al., 2019). Bottom currents can also generate gliding harmonic tremor signals at frequencies below 10 Hz, as currents above 5 cm/s interact with the OBS and cause resonance of protruding structures (Essing et al., 2021; Corela et al., 2023).

Various oceanic noise sources can also impact background noise levels on OBSs. This suggests that if clear relationships can be drawn between OBS noise and environmental factors, they could be used in a similar way to the frequency scanning method of Sit et al. (2012); potential tremor periods could be identified as times when ground velocities exceed that expected from environmental noise. Wind speeds, for one, have been shown to increase microseismic noise from very short period ocean waves and can saturate frequencies of 4-30 Hz. Above a given wind speed, noise levels are thought to rise without limit, potentially due to spray off whitecaps as wind waves break at the surface (McCreery et al., 1993). Bottom current speeds must also be considered; Tréhu (1985) showed that, at frequencies below 10 Hz, seismic noise levels increase proportionally with the square of bottom current speeds. However, there are also seasonal patterns in background noise due to marine mammal calls, which affect the ~14-30 Hz band in the wintertime in the northeast Pacific (Andrew et al., 2011; Curtis et al., 1999). This could disrupt environmental noise relationships and complicate frequency scanning methods.

In Cascadia, there is extensive tectonic tremor in the deep downdip portion of the subduction zone (Wech, 2021), but it has not been observed offshore in the shallow subduction zone. Full shallow locking along the majority of the margin is suggested by a lack of offshore seismicity on the plate interface (Morton et al., 2023; Stone et al., 2018) and initial GNSS-acoustic observations near the deformation front (DeSanto et al., 2025). Offshore resolution of geodetic models near the deformation front is poor, but there is some evidence of only partial locking offshore Oregon (Burgette et al., 2009; Li et al., 2018; Schmalzle et al., 2014). In this same region, near ~44.5°N, some of the only offshore seismicity located on the plate interface has been attributed to subducted seamounts (Carbotte et al., 2024; Morton et al., 2018; Tréhu et al., 2015) and very low frequency earthquakes have been reported (Chaudhuri and Ghosh, 2022). Serendipitously, this is the site of one of the longest continuous deployments of seismometers in offshore Cascadia: two broadband OBSs have been in operation since 2015 on the Ocean Observatories Initiative (OOI) Regional Cabled Array (Figure 1). The OOI OBSs are at an ideal station spacing for joint detection of tremor (~20 km), and are buried, which may reduce noise levels (Duennebier and Sutton, 2007). Given the evidence that this portion of the margin may only be partially locked, we focus on these two stations to search for evidence of shallow tectonic tremor.

In this paper, we first take advantage of the OOI cabled instrumentation, which includes in situ bottom current measurements, to investigate the relationship between buried OBS noise and environmental noise in Cascadia. We demonstrate the advantages of OBS burial and explore whether relationships between OBS noise and wind or bottom current speeds could be used to distinguish periods of active tremor. Then, motivated by the global need for a flexible seafloor tectonic tremor detection method, we develop a single-station approach to identify individual tectonic tremor signals on a single OBS amidst the presence of T-phases and ship noise. This is particularly important offshore Cascadia, which is a major shipping corridor (Dahl et al., 2021) close to multiple transform faults and mid-ocean ridges, which generate many T-phases (e.g., Dziak et al., 2011; Liu and Tan, 2025; Shen and Wu, 2023). We validate this technique using an existing offshore tectonic tremor dataset from a network of OBSs in the Hikurangi subduction zone and the NoMelt OBS network in the central Pacific, where no tremor is expected. We then apply our approach to the OOI dataset for 2015-2024 to explore whether shallow tectonic tremor occurs offshore Cascadia near ~44.5°N.

2 Data

2.1 Cabled OOI seismometer and hydrophone data

Beginning in late 2014, the Ocean Observatories Initiative (OOI) Regional Cabled Array came online with five cabled three-component ocean bottom seismometers (OBSs) at two sites near the deformation front of the Cascadia subduction zone at ~44.5°N (Figure 1) (Kelley et al., 2016; Smith et al., 2018; Trowbridge et al., 2019). At 2920 m depth, the Slope Base site lies 5 km west of the deformation front and is instrumented with one broad-

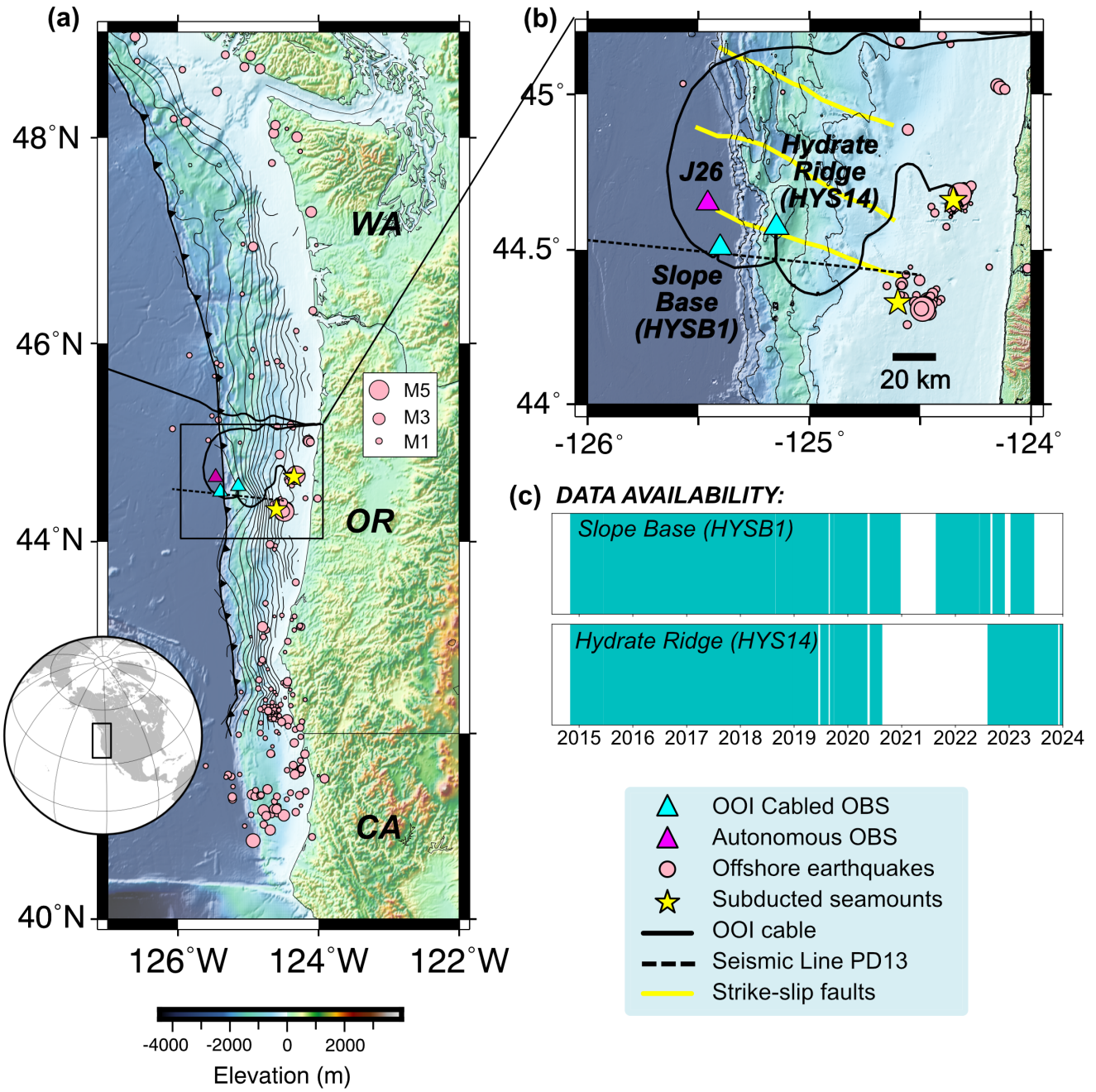

Figure 1 **(a)** Map of the Cascadia subduction zone with deformation front and subducting plate interface contours from Carbotte et al. (2024), shown at 1 km intervals. Earthquakes from Stone et al. (2018) and Tréhu et al. (2012) are shown as pink circles scaled by magnitude; the largest earthquake shown is M4.9. The inferred locations of subducted seamounts, which mark the two main seismicity clusters on the plate interface, are shown with yellow stars. The OOI cable is shown with a thick black line and the cabled OBSs are shown as cyan triangles. The autonomous OBS from the Cascadia Initiative nearest to Slope Base, station code J26D, is shown with a magenta triangle. Seismic line PD13 from the CASIE21 survey is shown with a dashed line (Canales et al., 2023). **(b)** Zoomed map focused on the deformation front near ~44.5°N. Contours show bathymetry at 500 m intervals. Nearby strike-slip faults from Goldfinger et al. (1997) are shown with yellow lines. Fault names from north to south are Wecoma, Daisy Banks, and Alvin Canyon. All other symbols follow (a). **(c)** Data availability of the two stations we focus on in this study, with times of available data marked by cyan bars.

band seismometer (station code HYSB1). Just ~20 km east, at 790 m depth, the Southern Hydrate Ridge site hosts a second broadband seismometer (HYS14). Both broadband seismometers are Guralp CMG-1T sensors co-sited with a High Tech HTI-90-U hydrophone. The seismometers and hydrophones all sample at 200 Hz, and the seismometers are buried at < 1 m depth. The seismometers were deployed with a remotely operated vehicle that created a shallow hole by inserting a caisson into the sediments, removing sediment from within the caisson, placing the seismometer within while ensuring that it was not touching the caisson, and then burying the instrument in glass beads (following Romanowicz et al., 2006). At the Southern Hydrate Ridge site, there are also three Guralp CMG-6TF short period seismometers located ~0.5 km to the northwest, north-

east and southeast of station HYS14, with station codes HYS11, HYS12, and HYS13, respectively. Because these are essentially co-sited with HYS14, we only use these instruments for manual checks of signal occurrence. We focus on the two broadband stations, HYSB1 and HYS14.

Both HYSB1 and HYS14 have good quality data beginning in February 2015 (Figure 1c). The instruments recorded nearly continuously, with occasional short outages mainly due to network outages, maintenance, and Navy diversions, until August 2020. HYSB1 resumed recording in August 2021 and continued, amidst several outages, until January 2024, when communications were lost with the junction box. HYS14 resumed recording in August 2022 and continued into 2024. We analyze all data up to January 2024.

2.2 Autonomous seismometer data

To validate our approach, we use data from autonomous OBSs deployed offshore New Zealand in the Hikurangi subduction zone. The HOBITSS experiment deployed 15 OBSs around a subducting seamount to capture a shallow slow slip event that occurred during September and October 2014 (Wallace et al., 2016). Todd et al. (2018) used nine of these OBSs to create a catalog of shallow tectonic tremor associated with the slow slip event. The instruments were not buried. The instruments with station codes starting with "LOBS" are broadband Nanometrics Trillium Compact seismometers that sample at 100 Hz, while the instruments with "EBS" station codes are short period Lennartz LE-3Dlite seismometers that sample at 200 Hz.

We also validate our approach on an autonomous OBS dataset in the central Pacific, which is not expected to include tectonic tremor. The NoMelt experiment deployed 22 broadband OBS for one year, January 2012-January 2013, to support seismic imaging of the base of the lithosphere (Lin et al., 2016). The instruments are broadband Trillium-240 seismometers that sample at 50 Hz. They were not buried.

2.3 Bottom current data

At both the HYSB1 and HYS14 sites, bottom currents are measured using a cabled 3-D Nobska MAVS-4 single point velocity meter. Water velocity (both speed and direction) is measured at a height of ~1 m from the seafloor and reported once per minute. We take the vector sum of the north and east components of water velocity to yield horizontal bottom current speeds at each site. The bottom current data is prone to clipping, so we remove any measurements greater than 0.5 m/s and calculate an hourly median value (Figure S1a). Bottom current data is available continuously at both sites at the same times as the seismometers, but data quality is compromised for significant time periods and not all available data has been verified (see Figure S1a). Here, we focus on one year of data from July 2018-July 2019, during the longest period that both sites have good quality data.

2.4 Wind speed data

We retrieve wind speeds from the ERA5 global reanalysis, which combines observations with models to create a hindcast of atmospheric, land surface, and oceanic parameters from 1950 onwards (Hersbach et al., 2020). We use the two horizontal components of wind, which are calculated at 10 m above earth's surface at hourly time steps and a horizontal resolution of 0.25° latitude by 0.25° longitude. We linearly interpolate the gridded data to the HYSB1 and HYS14 sites and take the vector sum of the two horizontal components to yield hourly horizontal wind speeds for each site (Figure S1b).

3 Methods

3.1 Environmental modeling to define background noise sources

We attempt to model smoothed amplitudes of the HYSB1 and HYS14 seismic time series using wind speeds from ERA5 reanalysis and bottom current speeds recorded at each site. We do this separately for two frequency bands of interest. We assume amplitudes in the 3-10 Hz band are representative of tectonic tremor, while amplitudes from 10-25 Hz are representative of other signals, including whale calls (e.g., Wilcock et al., 2014). The minimum frequency of 3 Hz is chosen to minimize the impact of microseismic noise. We calculate hourly median amplitudes of absolute ground velocities with a 50% overlap. For both the HYSB1 and HYS14 stations, we retrieve one hour of data for all three components at a time, padded by 5 minutes on either end. We demean the raw time series, apply a Butterworth bandpass filter, scale the data by the average instrument response in the frequency band, trim the padding on either end, and then take the absolute value of the data. We take a vector sum of the two horizontal channels and then record the median amplitude of the vertical and horizontal data for that hour. Due to occasional network outages, there are some periods of missing seismic data; we infill these times by linearly interpolating between data points. We then smooth the median seismic amplitudes, wind speeds, and median bottom currents, all of which are hourly time series, using a Gaussian filter with a standard deviation of 8 hours. After smoothing, we mask periods of data outages; these data points are ignored in modeling.

We create separate models for wind speeds and bottom currents using an approach that is intended to be robust against outliers. Depending on frequency, seismic noise levels are expected to either saturate at low wind speeds and then rise without limit past a higher threshold, or saturate only once a higher threshold is reached (McCreery et al., 1993). Therefore, following Hilmo and Wilcock (2020), we use wind speeds to model smoothed seismic amplitudes as a piecewise function:

$$\begin{aligned} m_t &= b_1 + c_1 w_t \; for \; w_t < B \\ m_t &= b_2 + c_2 w_t \; for \; w_t \geq B \end{aligned} \tag{1}$$

where m is the modeled ground velocity, t is an index of discretized time, w is wind speed, B is the threshold

wind speed that acts as a breakpoint for a piecewise linear function with two segments, and b_1, b_2, c_1 and c_2 are constants. For a given hinge point (w_{test}, $B_{test,}$), we fit both portions of the data, $wt < B_{test}$ and $w_t >= B_{test}$, with a line that intersects the hinge point. On either side of the hinge point, we vary the slope of the line and choose that which gives the center of the narrowest band enclosing half the points in the y-direction (see Figure S5). We do not allow negative slopes. We perform a grid search over a small range of values surrounding a visually estimated hinge point and choose the hinge point B that minimizes the weighted average of the two band widths. If no hinge point is visually apparent, we fit the data with only one line.

Tréhu (1985) showed that, at frequencies below 10 Hz, seismic noise levels appear to increase proportionally with the square of bottom current speeds; this relationship was derived using an OBS that was specifically designed to minimize bottom current interactions and avoid strumming and vortex shedding. Therefore, using bottom currents, we model smoothed seismic amplitudes as:

$$m_t = b + cs_t^2 \tag{2}$$

where m is the modeled ground velocity, t is an index of discretized time, s is horizontal bottom current speed, and b and c are constants; we do not allow c to be negative. To fit the model, we solve for the line that is the center of the narrowest band enclosing half the points in the y-direction (Figure S5). For both wind speed and bottom current models, we do not report R values as in previous studies, which estimate how well a model can explain observed variation in the data (Hilmo and Wilcock, 2020). This value is only meaningful when model misfits are normally distributed after a least squares minimization, which is not our case.

3.2 Detection and classification of emergent signals

3.2.1 Envelope cross-correlation

To test the performance of envelope cross-correlation between the two broadband seismometers at the HYSB1 and HYS14 sites, we follow the method of Wech et al. (2013), who focused on OBSs. We process 24 hours of data at a time with 5 s of padding on either end. Using a horizontal channel from each instrument, we first taper the 5 s on both ends of the data using a Hann window, and then apply a 4-corner minimum phase 3-10 Hz Butterworth bandpass filter to minimize the impact of microseismic noise and to isolate the expected frequency of tremor. We take an envelope of the filtered data and apply a 5-s low-pass filter. The enveloped data is decimated to 1 Hz and the padding on either end is trimmed to avoid edge effects. We cross-correlate 300-s windows with 50% overlap. We allow a maximum shift of 10 s, which conservatively accounts for the maximum lag we would expect if S-waves are travelling horizontally 20 km between stations. We save the maximum cross-correlation value of each window to determine windows that likely include tremor.

3.2.2 Single-station emergent signal detection and classification

To detect tremor-like signals on a single station, we first isolate all emergent signals, and then apply waveform and spectral requirements to leave only those consistent with tectonic tremor (see flow chart in Figure 2). To find emergent signals, we first perform short-term average long-term average (STA/LTA) triggering on one channel at a time. We use the horizontal components and process 24 hours of data at a time with an extra 1000 s at the start to account for the long-term window. Prior to triggering, we pad the data by 5 s on either end, taper the padded data using a Hann window, apply a 4-corner minimum phase 3-10 Hz Butterworth bandpass filter, and trim the padding. We found that a short-term window of 10 s and a long-term window of 1000 s, with triggering on/off thresholds of 2/1, captures emergent signals of varying duration and excludes impulsive signals such as local earthquakes. Any detections with a duration less than 30 s are discarded.

To identify obvious T-phases, we determine the number of waveform peaks in each detection. Regional T-phases typically have one prominent peak in their smoothed waveform, whereas tectonic tremor typically exhibits multiple peaks. To smooth the waveform, we take the square of the 3-10 Hz filtered data, apply a 1-dimensional Gaussian filter with a standard deviation of 1.875 seconds, and normalize the data using its maximum. We then calculate the number of peaks in the waveform, between the trigger on/off times, with a prominence exceeding 0.1. If the smoothed waveform only has one peak, we categorize it as a T-phase (Figure 2a).

To assess whether the detection likely includes ship noise, we analyze the spectral characteristics. Ship noise is typically identified by monochromatic bands of energy (Ross and Kuperman, 1989). We identify whether this is present by first estimating the power spectrum of the unfiltered signal using Welch's method with a 1-s segment length, Hann taper, and 50% overlap (Welch, 1967). To avoid misidentifying peaks related to microseismic noise, we discard the portion of the power spectrum related to the microseism, which we conservatively take as all frequencies below 4 Hz. We convert the spectrum to decibels and then identify any peaks in the power spectrum that are greater than the median power between 20-80 Hz and have a prominence greater than 10 dB. If there are any peaks that meet these requirements, we determine that the detection likely includes ship noise (Figure 2b).

To determine whether the detection exhibits a significant decrease in spectral power above 10 Hz, as expected for tectonic tremor, we calculate a ratio between low and high frequency amplitudes (hereafter referred to as F_{LH}). We first pad the detected signal by 30 s on either side of the trigger on and off times, which accounts for times that our detector occasionally captures only the start of a long-duration T-phase arrival or noise signal. The 30 s padding ensures that the complete spectral characteristics of the signal are captured. We then estimate the power spectrum using Welch's method with a

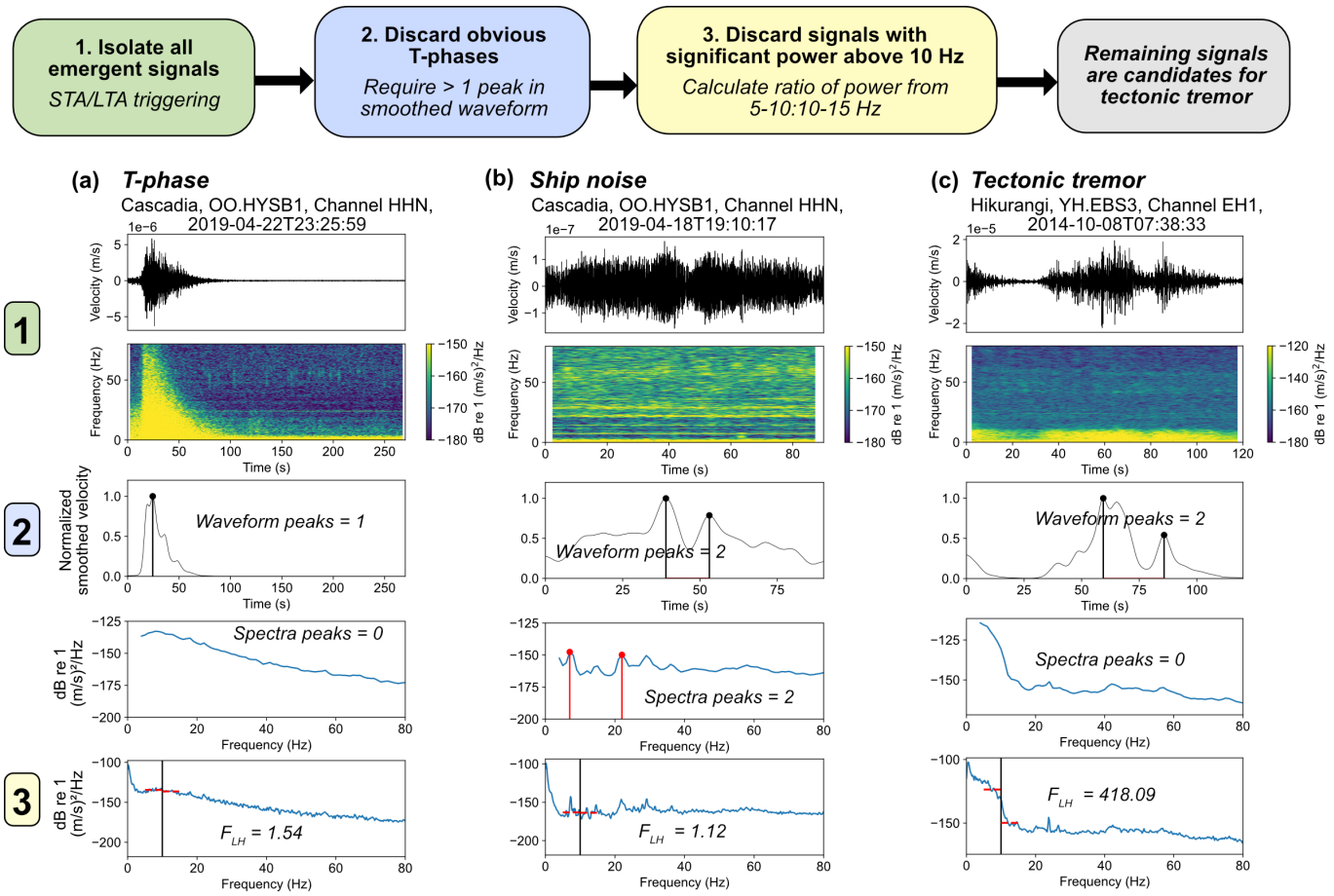

Figure 2 Flow chart illustrating the logic of our single-station tremor detection approach, with results of analysis for three different signals detected using STA/LTA (Step 1): **(a)** T-phase in Cascadia, **(b)** ship noise in Cascadia, and **(c)** tectonic tremor in Hikurangi. The title of each subplot lists the station code, channel, and the start time of the window. The first row of each subplot shows the waveform of the signal bandpass filtered from 3-10 Hz and the second row shows a spectrogram of the same waveform. The third row shows results of peak picking on the smoothed waveform (Step 2): 1 peak indicates a T-phase (a), while > 1 peak indicates a potential tremor-like signal (b and c). The fourth row shows the results of peak picking in the spectra: the presence of peaks indicates ship noise (b). This is experimental and not applied in tremor detection. The final row demonstrates the calculation of F_{LH}, or the ratio between power in the 10-15 Hz band and the 5-10 Hz band (Step 3). Signals consistent with tectonic tremor are expected to have a larger F_{LH} (c).

5-s segment length, Hann taper, and 50% overlap. We compute F_{LH} as the ratio between the median of power between 5-10 Hz and the median of power between 10-15 Hz. For tectonic tremor signals, we expect that F_{LH} will be higher than for non-tectonic tremor signals (i.e., Figure 2c). The F_{LH} threshold used to identify potential tectonic tremor detections is described in Section 4.

We tuned these analyses on subsets of 200 STA/LTA detections from each OOI station that we visually identified as T-phases and ship noise (see Text S1). We used existing detections from Hikurangi to inform expected waveform characteristics of tectonic tremor (no clear single peak and diminished power above 10 Hz; Figure 2c). An illustration of these three analyses, applied to representative examples of T-phase, ship noise, and tectonic tremor detections, is shown in Figure 2. We classify a detection as a T-phase if it has only one waveform peak (Figure 2a). We classify a detection as potential tectonic tremor if it has more than one waveform peak and has an F_{LH} higher than a chosen threshold (Figure 2c). If we identify that a detection contains ship noise (Figure 2b), it may also be classified as a T-phase or potential tectonic tremor, or neither; ship noise, particularly in the region of the OOI, often overlaps other signals.

4 Results

4.1 Environmental modeling

We find an overall weak and variable relationship between environmental factors and background noise on the OOI OBSs, which prevents us from using them as a proxy to identify periods of potential tremor. For wind speeds, we observe a relationship to seismic ground velocities at both sites, but we do not consistently observe saturation of noise at a threshold wind speed as expected (Equation 1). At Slope Base, the strongest relationship between wind speeds and seismic ground velocities is observed at 3-10 Hz, with a stronger relationship in the horizontal component (Figure 3a-b). The best fit model gives a saturation wind speed of 7.5 m/s and 6.6 m/s for the horizontal and vertical components, respectively. There is no relationship between wind

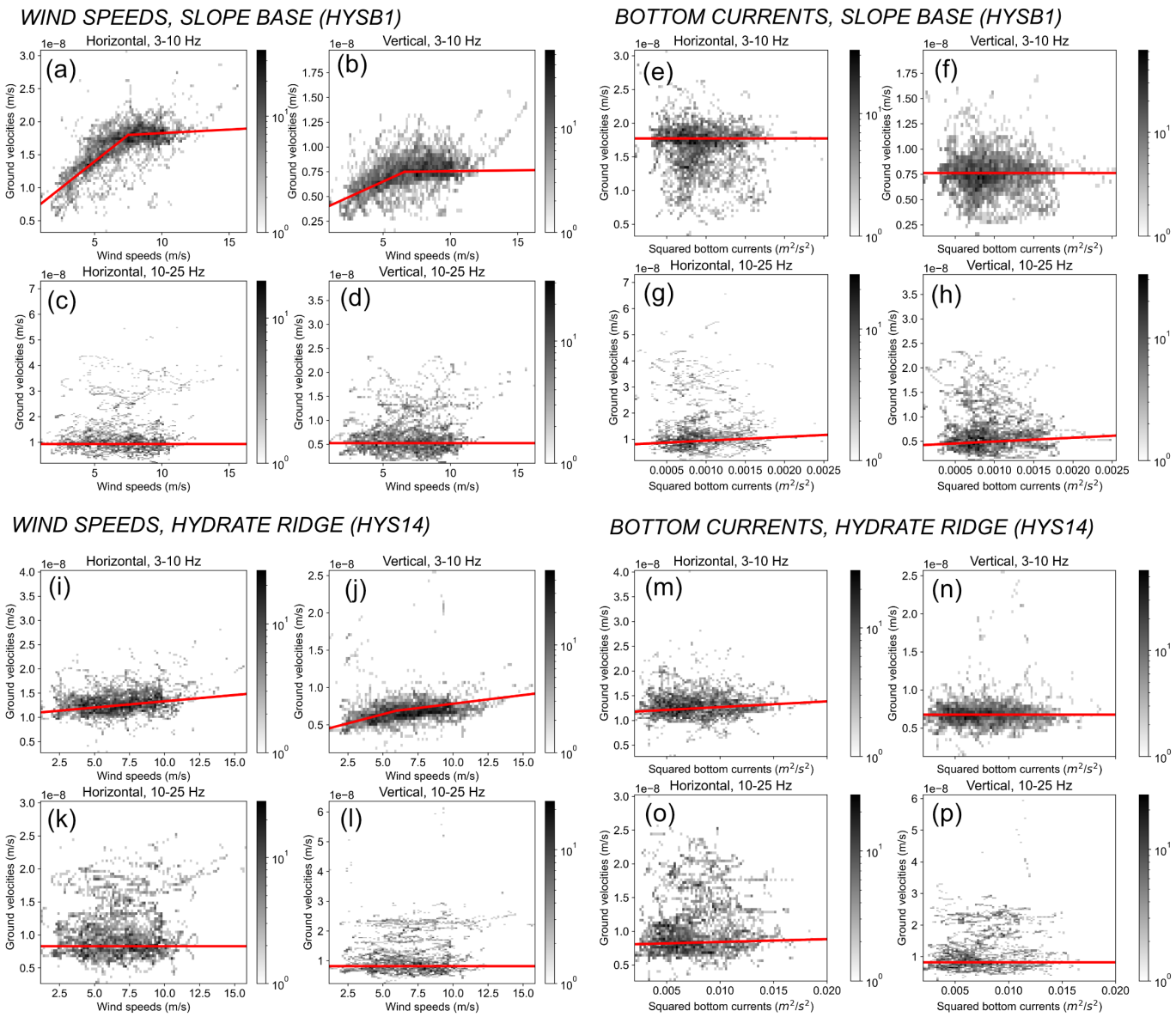

Figure 3 Results of environmental modeling of seismic ground velocity amplitudes. Density plots, shown as 2-D histograms, show the relationship between smoothed hourly environmental time series (x-axis) and smoothed hourly median seismic ground velocities (y-axis) for different frequency bands and seismometer components. The gray scale shows the number of points, one per hour, per 2-D bin on a logarithmic scale. **(a-d)** Modeling of seismic ground velocities using wind speeds at the Slope Base (HYSB1) station. The robust piecewise model (Equation 1) is shown as a red line. Bin dimensions are 0.15 m/s by 0.04e^{-8} m/s. Here and in the remaining subplots, results are shown for horizontal and vertical components in the 3-10 Hz and 10-25 Hz frequency bands. **(i-l)** Same as (a-d) but for the Hydrate Ridge (HYS14) station. **(e-h)** Modeling of seismic ground velocities using squared bottom currents at the Slope Base (HYSB1) station. The best-fit model (Equation 2) is shown by a red line. Bin dimensions are 0.0003 m^2/s^2 by 0.04e^{-8} m/s. **(m-p)** Same as (e-h) but for the Hydrate Ridge (HYS14) station, with bin dimensions of 0.0002 m^2/s^2 by 0.04e^{-8} m/s .

speeds and seismic ground velocities at Slope Base in the 10-25 Hz band (Figure 3c-d). Both the horizontal and vertical components do not display an obvious saturation wind speed and our robust model fitting gives a line with zero slope. We note that in all the plots for 10-25 Hz, there are outliers which are due to seasonal fin whale calls in the fall and winter centered at 18-22 Hz.

The relationship between wind speeds and seismic ground velocities is overall weaker at Hydrate Ridge. Only the vertical component in the 3-10 Hz band appears to display a weak break at a saturation wind speed of 6.0 m/s (Figure 3j). The horizontal component in the 3-10 Hz band shows no clear saturation point and is fit using a single line (Figure 3i), while both components in the 10-25 Hz band show no dependence on wind (Figure 3k-l).

We observe very little to no relationship between seismic ground velocity amplitudes and in-situ measured bottom currents at either the Hydrate Ridge or Slope Base sites. At Slope Base, there is no relationship in either component in the 3-10 Hz band and only a very weak apparent dependence at 10-25 Hz (Figure 3e-h). At Hydrate Ridge, the only apparent weak dependence is observed on the horizontal components (Figure 3m-p).

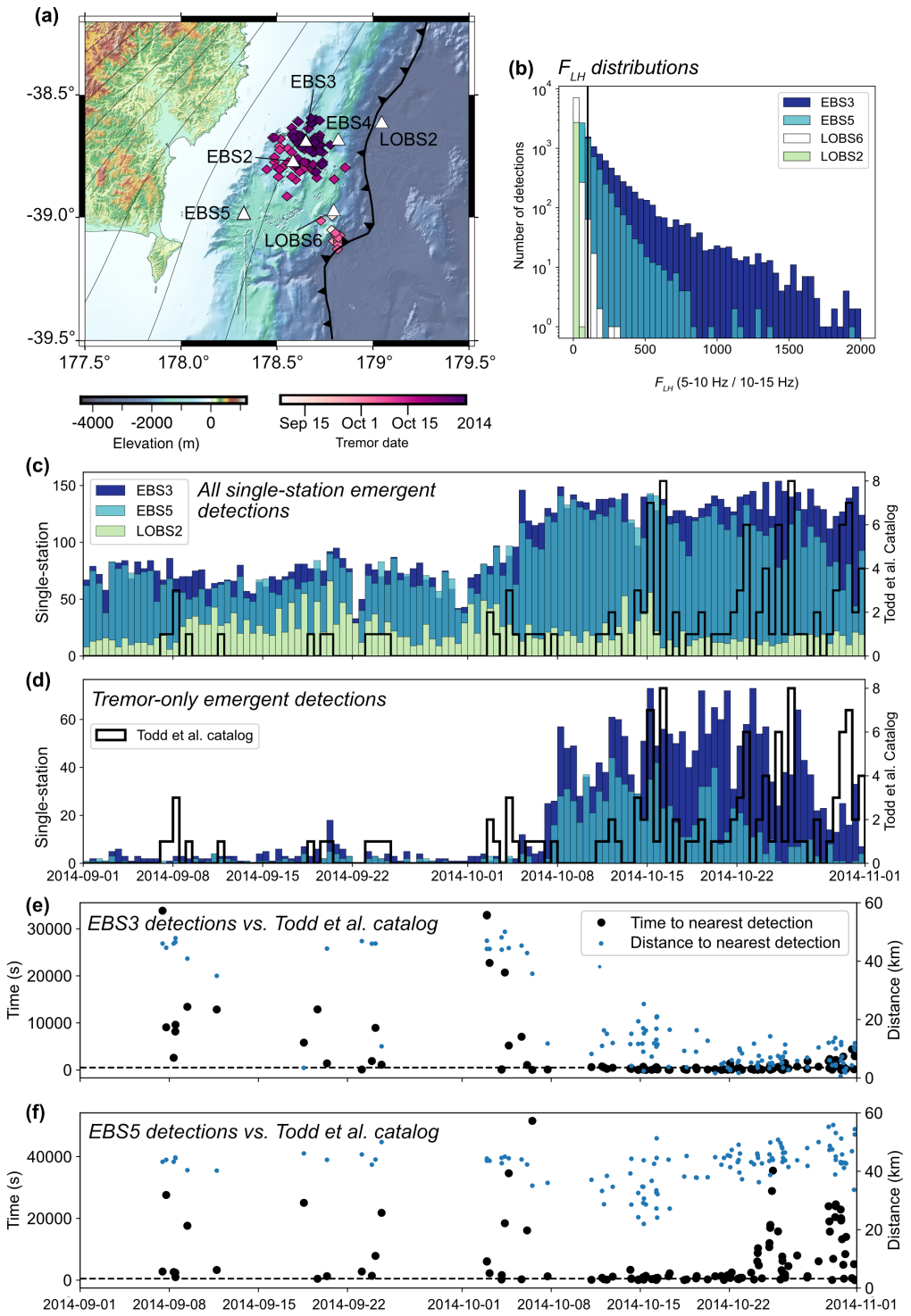

Figure 4 Performance of our single-station STA/LTA detection and classification method on OBSs with cataloged tectonic tremor in the Hikurangi subduction zone. **(a)** Map showing the OBSs we used from the HOBITSS network as white triangles with station names annotated. Tectonic tremor localizations from Todd et al. (2018) are shown as diamonds colored by time. The deformation front and subduction slab depth contours at 3 km intervals (Hayes et al., 2018) are shown as black lines. **(b)** Histogram showing distribution of F_{LH} values for all single-station detections for a subset of HOBITSS OBSs. The black vertical line at F_{LH} = 100 denotes the cut-off we use to classify detections as tremor. Note the y-axis log scale. **(c)** Histogram showing time distributions of single-station STA/LTA detections for stations EBS3, EBS5, and LOBS2 for September-October 2014 as colored bars, overlain by the time distribution of tectonic tremor localizations from the Todd et al. (2018) as thick black lines. Note the two different y-axes. **(d)** Same as (c), but only showing single-station detections we classify as tremor (more than one peak in the smoothed waveform and F_{LH} > 100). Note that there are no tremor detections for station LOBS2. **(e)** Tremor detections from Todd et al. (2018) and STA/LTA for the EBS3 station. Black circles show the minimum time between each detection of Todd et al. (2018) and an STA/LTA detection, plotted on the left axis. Blue dots show the spatial distance between each detection of Todd et al. (2018) and station EBS3, plotted on the right axis. There is one blue circle and one black dot per detection of Todd et al. (2018). The horizontal dashed line corresponds to a timing difference of 500 s. **(f)** same as (e) but for station EBS5.

4.2 Comparison of envelope cross-correlation and single-station STA/LTA triggering

We compare the performance of envelope cross-correlation and single-station STA/LTA triggering methods for the HYS14 and HYSB1 stations from July 2018-July 2019 (Figure S6), in order to identify which method is more appropriate to search for small tectonic tremor signals. We use both horizontal channels, HHN (North) and HHE (East), for these comparisons and we also compare each method between channels. For envelope cross-correlation between the two sites, we consider detections as windows with cross-correlation values greater than 0.7.

The temporal pattern of emergent signal detections is similar between envelope cross-correlation and single-station STA/LTA detection, and the results are also very similar between channels (Figure S6). On the HHN channels, envelope cross-correlation yields 4,581 detections, while single-station STA/LTA triggering yields 4,098 and 12,348 detections on HYSB1 and HYS14, respectively. On the HHE channels, envelope cross-correlation yields 4,889 detections, while single-station STA/LTA triggering yields 4,380 and 12,246 detections on HYSB1 and HYS14, respectively. We only use the HHN channels going forward.

There is significant overlap between envelope cross-correlation and single-station STA/LTA triggering results. On the HHN channels, 94% and 85% of the envelope cross-correlation detections overlap with an STA/LTA detection on HYS14 and HYSB1, respectively. Visual inspection of a subset of 100 envelope cross-correlation detections reveals that > 65% are clear T-phases, showing that the method does not effectively filter out non-tremor signals. Although the single-station method also detects many T-phases, it is simpler to identify T-phases within STA/LTA detections because detections are centered on the signal. Further, STA/LTA detection also allows for the case where only one station records a signal, which is important given the difference in number of emergent signals across stations (Figure S6). We therefore proceed with single-station STA/LTA triggering to detect small tremor signals.

4.3 Single-station method validation offshore Hikurangi and in the central Pacific

To demonstrate that our approach of single-station STA/LTA triggering and subsequent detection classification (Figure 2) effectively identifies tectonic tremor on OBSs, we apply the method to data from the Hikurangi subduction zone for which there is a published catalog of tectonic tremor (Todd et al., 2018) (Figure 4). The tectonic tremor catalog was constructed using envelope cross-correlation with a requirement for correlation coefficients > 0.6 across at least 7 stations. We cannot expect our tremor detections to correlate perfectly with the Todd et al. (2018) catalog because our method uses only a single station; instead, if our method is successful, we may expect many more detections on an individual station but an overall temporal trend that mimics the Todd et al. (2018) catalog. We used data from six of the OBSs used by Todd et al. (2018), selected for their varying distance from the locus of tremor: stations EBS2, EBS3, EBS4, EBS5, LOBS2, and LOBS6 (Figure 4a).

We present results for three OBSs that are representative of overall patterns (Figure 4). Station EBS3 is essentially atop the main tremor patch, while stations EBS5 and LOBS2 are both ~30-40 km away (Figure 4a). Station EBS5 is on the overriding plate at a similar depth to station EBS3 (~1000 m) while LOBS2 is located on the incoming plate at > 3000 m depth (Figure 4a). For September-October 2014, STA/LTA triggering identifies 12,314, 10,539, and 2,716 emergent signals on the EBS3, EBS5, and LOBS2 stations, respectively (Figure 4c). The number of overall STA/LTA detections increases markedly on the EBS3 and EBS5 stations in early October, but this trend is not seen on station LOBS2 (Figure 4c). Manual inspection of the LOBS2 data shows that, even for periods of tremor identified by Todd et al. (2018), tectonic tremor is not recorded at this station; instead, most of the STA/LTA detections appear to be T-phases.

To identify detections that are consistent with tectonic tremor, we first require that a detection have more than one peak in its smoothed waveform (Figure 2a). This removes 62%, 63%, and 61% of detections on EBS3, EBS5, and LOBS2, respectively. Because we are solely interested in the presence of tectonic tremor in this dataset, we do not check for ship noise (Figure 2b); the presence of ship noise does not preclude the presence of tremor. We then calculate the F_{LH} of all detections (Figure 2). We find that the two stations that record tectonic tremor, EBS3 and EBS5, have a much wider distribution of F_{LH} than the station that does not record tectonic tremor, LOBS2 (Figure 4b). LOBS2 has no detections with F_{LH} greater than 100. Visual checks show that almost all detections on EBS3 and EBS5 with $F_{LH} > 100$ appear to be tectonic tremor.

By requiring more than one peak in the smoothed waveform and a $F_{LH} > 100$, we find 2,403 tectonic tremor detections on EBS3, 966 on EBS5, and zero on LOBS2 (Figure 4d). Todd et al. (2018) observe several bursts of tremor in September 2014 and then more consistent and frequent tremor beginning in October 2014 (Figure 4d). The temporal trends of our tremor detections on EBS3 and EBS5 are in excellent agreement with these patterns (Figure 4d), suggesting that this approach effectively approximates the presence of tremor on a single OBS. Our approach finds approximately one order of magnitude more detections than Todd et al. (2018) (Figure 4d), almost certainly due to their requirement that the tremor signals be coherent across a minimum of 7 stations.

We find that there is much better timing agreement between individual tremor detections from Todd et al. (2018) and our single-station STA/LTA detections when the tremor source from Todd et al. (2018) is < 40 km from the recording station (Figure 4e-f). Prior to October 8, there are typically several hours between each tremor detection from Todd et al. (2018) and a STA/LTA tremor detection, suggesting that the STA/LTA method is detecting either a different tremor source or a different signal altogether when the tremor source is distant. Once tremor reaches closer to the instruments (<

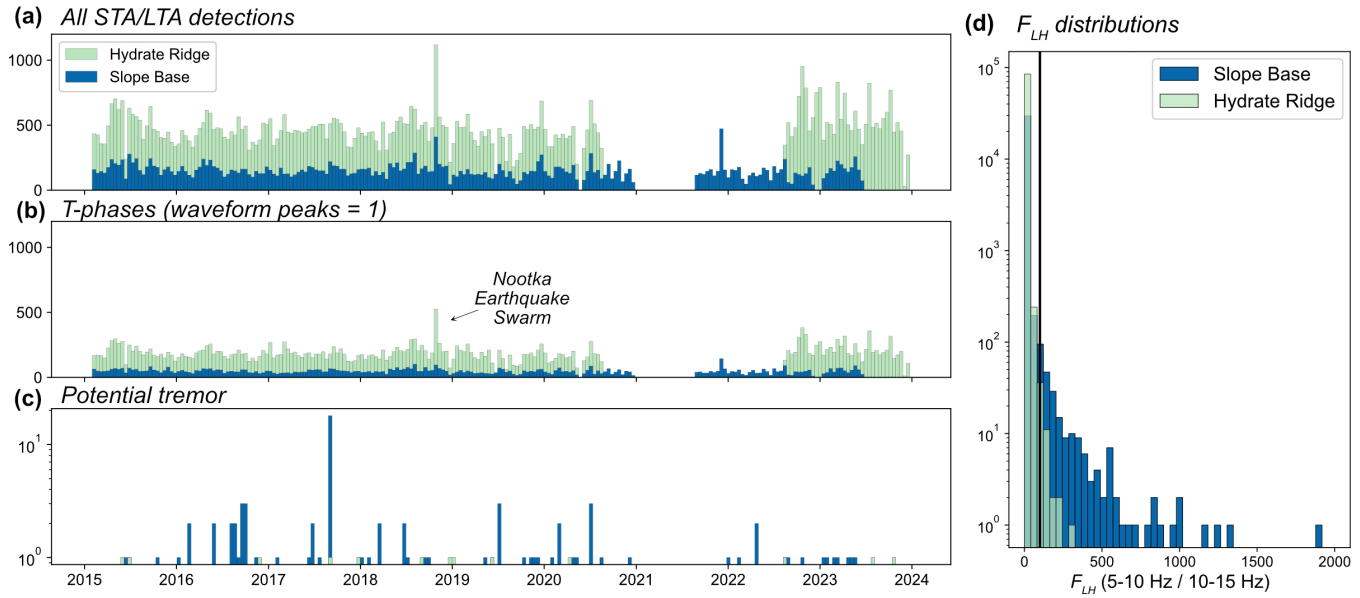

Figure 5 Results of single-station STA/LTA detection and classification on OOI stations HYSB1 (Slope Base) and Hydrate Ridge (HYS14). **(a)** Histogram showing number of detections at Hydrate Ridge and Slope Base over time with bin sizes of 2 weeks. **(b)** Same as (a) but only showing detections that have one peak in their smoothed waveform, indicating they are T-phases. The largest peak can be attributed to a swarm of earthquakes near the Nootka fault zone which generated many regional T-phases. **(c)** Same as (a) but only showing detections which have more than one waveform peak and F_{LH} > 100, indicating they are consistent with tectonic tremor. Note the log scale. **(d)** Histogram showing distributions of F_{LH} for all detections for both Slope Base and Hydrate Ridge. The black vertical line indicates the minimum value required for potential tremor, F_{LH} = 100. Note the log scale.

~40 km) around October 8, however, the typical timing difference between a tremor detection from Todd et al. (2018) and an STA/LTA detection drops to several minutes or less, suggesting the STA/LTA approach is detecting signals within the same tremor wave trains. In late October, the tremor source continues to migrate further from station EBS5 (> 40 km) but closer to station EBS3; correspondingly, the temporal agreement between the detections from Todd et al. (2018) and STA/LTA remains strong at station EBS3, but worsens at station EBS5 (Figure 4e-f). We verified that this improved temporal agreement is not simply due to an overall larger number of detections (Figure S7).

We find one station, LOBS6 (Figure 4a), dominated by bottom-current induced tremor (Figure S8). This signal is characterized by gliding harmonic frequencies and is not inferred to be related to tectonics, but instead results from the interaction of strong bottom currents and protruding structures on the OBS (Essing et al., 2021; Corela et al., 2023). Our STA/LTA method produced 7,444 detections on LOBS6 in the two months of investigation and frequently triggered on these signals. These detections have multiple peaks in their smoothed waveform and F_{LH} values that at times are above 100 (Figure 4b, Figure S8a), which precludes them from being discarded by our method. Our check for ship noise, designed to identify spectral banding, does appear to identify the harmonic character of the current induced tremors (Figure S8), suggesting that this approach could be explored to handle instruments that are prone to bottom current-induced tremors.

To validate that our approach does not erroneously detect tectonic tremor in datasets where it is not expected, we apply our method to three broadband OBSs from the NoMelt experiment in the central Pacific. The unburied instruments were deployed at depths > 5000 m, such that they are not exposed to strong bottom currents. Over the year-long dataset, we find only 37 STA/LTA detections in total across the three stations that are consistent with tectonic tremor (multiple peaks in smoothed waveform, F_{LH} > 100). These detections can be quickly visually identified as regional T-phases, short duration events (SDEs), or harmonic bottom-current generated tremor (see Section 4.5 for further description and Text S2 for detailed results). We therefore conclude that our method performs as desired for an OBS dataset that does not include tremor: the approach quickly isolates a small number of tremor-like signals, which can then be quickly visually checked to confirm that no tectonic tremor signals are recorded.

4.4 Detection and classification of emergent signals at Slope Base and Hydrate Ridge

Based on the success of our single-station method at Hikurangi, we apply the same approach to stations HYSB1 (Slope Base) and HYS14 (Hydrate Ridge) on the OOI for February 2015-January 2024. STA/LTA triggering detects 85,166 signals on HYS14 and 30,055 signals on HYSB1 (Figure 5a). Of these detections, 30% on HYS14 and 65% on HYSB1 likely include ship noise in the form of spectral banding. We then classify 40% of detections at HYS14 and 32% of detections at HYSB1 as T-phases (Figure 5b), which have only one peak in their smoothed waveform (Figure 2a). The largest peak in number of T-phases is coincident with a swarm of earthquakes near

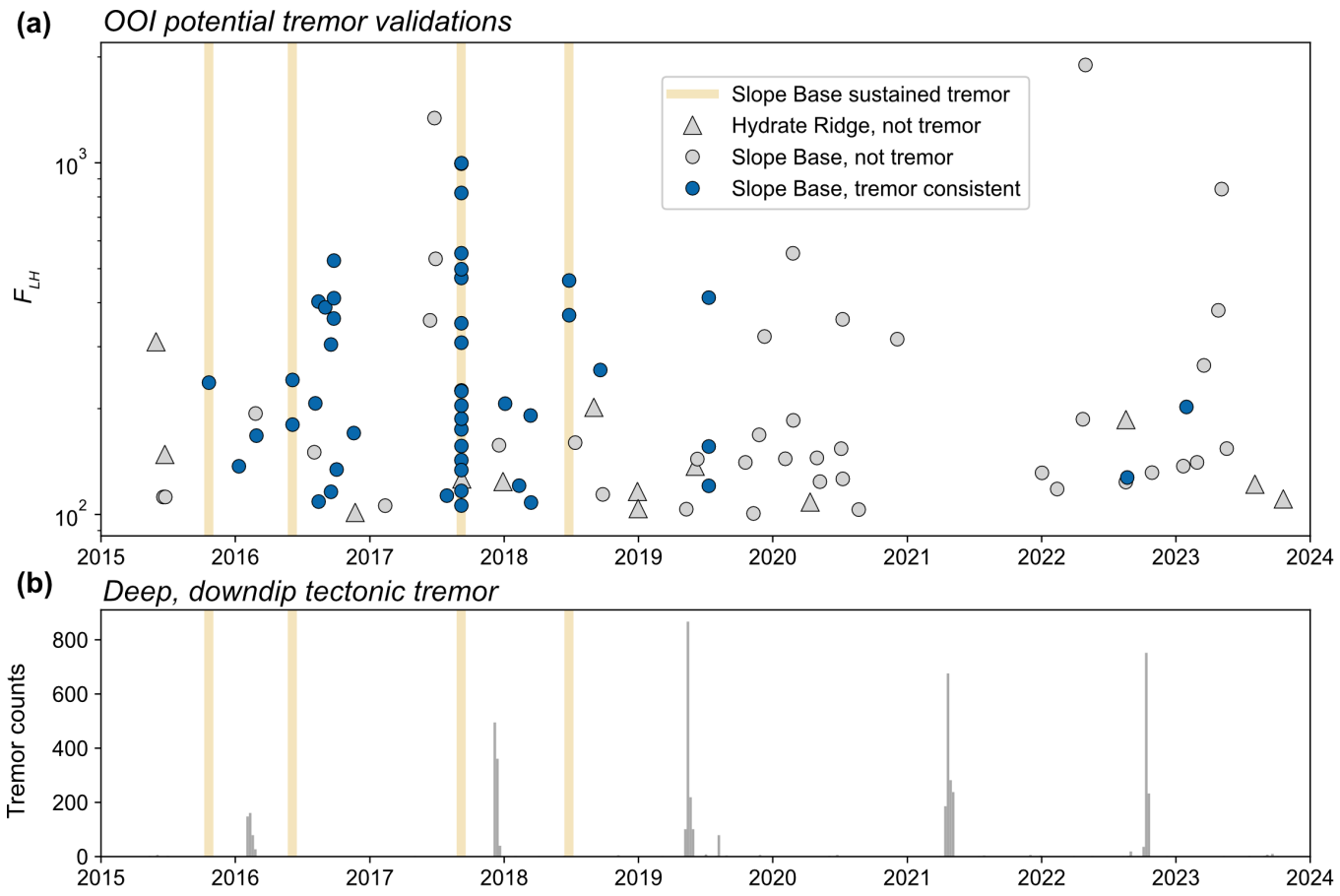

Figure 6 Results of visual inspection of all potential tremor signals at Slope Base and Hydrate Ridge. **(a)** Scatter plot showing the F_{LH} of all potential tremor detections over time for both stations (Figure 5c). Manually validated detections which are consistent with tectonic tremor are shown in blue (see Table S3 for exact times), and detections that are clearly not tremor shown in gray. The times when a tremor-like signal is observed at Slope Base for more than an hour are marked with yellow vertical lines (see Table S4 for exact times). **(b)** Histogram showing the number of downdip tremor detections over time in deep Cascadia, detected by the Pacific Northwest Seismic Network (Wech, 2010), between 44°N and 45°N and west of 123.5°W. Bin sizes are 1 week. Times of sustained tremor at Slope Base are again shown using yellow vertical lines.

the Nootka fault zone (Figure 5b).

To understand the overall spread of spectral characteristics, we calculate F_{LH} for all detections (Figure 5d). We find that detections at HYSB1 have a broader distribution of F_{LH} values in comparison to HYS14, with many more detections with $F_{LH} > 100$. As for our analysis at Hikurangi, we classify detections as potential tectonic tremor only if they have more than one peak in the smoothed waveform and $F_{LH} > 100$. We do not use the presence of ship noise to filter out detections because we found that ship noise was often present amidst other emergent signals (see Text S1). This leaves 86 potential tectonic tremor detections for HYSB1 and 13 for HYS14 (Figure 5c).

4.5 Visual investigation of potential tremor signals

We visually inspected all potential tectonic tremor detections on both HYSB1 and HYS14 to determine whether any show all characteristics expected for tectonic tremor (Figure 6a). We consider a detection to be consistent with tectonic tremor if it lacks energy above 10 Hz, shows multiple emergent peaks in the waveform, is not strongly recorded on the hydrophone as expected for T-phases (e.g., Figure S9a), and is not dominated by impulsive energy. Notably, no signals consistent with harmonic bottom current-generated tremor (e.g., Figure S8) were found on either instrument.

At station HYS14, we found that all potential tectonic tremor detections are consistent with regional T-phases: an overall spindle-like shape, evidence for some energy at frequencies > 10 Hz on the vertical channel, and a strong recording by the hydrophone (Figure S9a). We therefore conclude that no signals consistent with tectonic tremor are detected by our method on station HYS14 during 2015-2024 (Figure 6a).

In contrast, the potential tectonic tremor detections on HYSB1 do not include any T-phases. However, many detections consist of multiple impulsive peaks that primarily have energy < 10 Hz, abruptly appear and disappear and are not recorded on the hydrophone (Figure S9b). These characteristics are consistent with "short duration events" (SDEs), which are stereotypical noise signals that have long been observed on OBSs throughout the world's oceans at varying depths and settings (Tary, 2023), including offshore Oregon (Hilmo and Wilcock, 2020; MacLeod and Wilcock, 2025). SDEs

are inferred to be unrelated to earthquakes or other tectonic signals and instead have varyingly been attributed to biological activity (Buskirk et al., 1981) or the movement of gas bubbles through sediments underlying the instrument (Batsi et al., 2019; Tary et al., 2012). They are characterized by their short duration of < 5 s, a single phase arrival and dominance of a narrow frequency band, and are typically recorded on only one OBS at a time and not on the hydrophone (Tary, 2024). We find that 28 of the HYSB1 detections show this behavior (e.g., Figure S9b) and we classify them as non-tremor (Figure 6a).

We identify 47 detections from HYSB1 that do not appear to be SDEs, T-phases, or instrument noise and are instead consistent with the characteristics expected for tectonic tremor (Table S3; Figure 6a). In contrast to T-phases, detections do not have significant energy above 10 Hz, are not strongly recorded by the hydrophone, and lack a spindle-like shape (Figures 7-9 and S9). In contrast to short-duration events, energy at frequencies < 10 Hz is present continuously. The signals are also not dominated by spectral banding. For each of these tectonic tremor-like detections, we verified that the signal is not also recorded at HYS14 (Figures 7 and S9) or any of the collocated short-period stations HYS11-13.

Inspection of the time periods surrounding these tectonic tremor-like detections identifies four times when tremor appears to be sustained for at least one hour (Table S4; Figure 6a). During these periods, STA/LTA detections occur on individual emergent signals within the apparent sustained tremor (Figure 7). The four periods of sustained tremor are shown in their entirety in Figure S10 and contain 23 of the 47 tectonic tremor-like STA/LTA detections. The sustained tremor periods vary in duration from 1 hour to 7 hours (Table S4). For all four periods, the signal is recorded strongly on all channels (HHN and HHZ are shown in Figure 7). The signal appears to be partially recorded on the hydrophone, though not strongly, and only during times when the frequency content "spikes" above 10 Hz (Figure 7). The sustained periods of tremor typically start with a strong emergent signal on the seismometer, and then fade into what appears to be a background saturation at frequencies < 10 Hz, interspersed with additional strong emergent signals and, occasionally, impulsive signals that are also recorded on the hydrophone (Figure 7). During the longest period of sustained tremor, in September 2017, there are gliding harmonics during the period of strongest tremor (Figure S10c).

The remaining 24 of the visually validated tremor-like STA/LTA detections occur as isolated tremor bursts (Figures 9b and S11). These signals are generally quieter than those observed during the four sustained periods. They generally do not contain impulsive signals and are not recorded on the hydrophone. The highest concentration of isolated tremor signals is observed in late 2016 (Figure 6a), but otherwise, they display no clear temporal pattern.

5 Discussion

5.1 The significance of instrument burial

We do not observe harmonic bottom current-induced tremor signals on the buried OOI instruments, despite high bottom current speeds (up to 0.3 m/s, Figure S1). This is in stark contrast to an unburied OBS very near HYSB1, where we found that bottom current-induced tremors dominate records (station J26D, Figure 1; see Section 5.2 for more details). We did not explore a solution for classifying harmonic bottom current-induced tremor, but it would be necessary for working with unburied OBSs in Cascadia or elsewhere. As we have shown for OBSs in Hikurangi, bottom current-induced tremor can be particularly disruptive for single-station detection of tectonic tremor (Figure S8). Similarly to our identification of ship noise, peaks in spectra could potentially be used to identify the harmonic nature of bottom current-induced tremor.

For both HYSB1 and HYS14, the relationship between background noise levels and in situ measured bottom currents is either weak or nonexistent (Figure 3). The relationship is not clearly stronger on the horizontal channels, as expected for unburied instruments (e.g., Tréhu, 1985). Past studies showed that OBS burial only a short distance beneath the ocean floor could strongly reduce noise (Collins et al., 2001; Duennebier and Sutton, 2007). These studies directly compared measured bottom currents and OBS noise and reported that burial of instruments reduced current-related noise below 1 Hz, for currents up to 0.1 m/s. We show that burial also reduces current-related noise at higher frequencies relevant to tectonic tremor and body waves from regional and local earthquakes, and we also show that this relationship stands up to bottom current speeds of 0.3 m/s (Figures 3 and S1).

OBS burial does not remove the influence of wind speeds on overall OBS noise, although the relationships we observe are variable (Figure 3). Interestingly, the deeper HYSB1 station shows a much stronger relationship to wind than HYS14 (Figure 3), despite similar wind speeds (Figure S1). One potential reason for this is that the Slope Base site is located 20 km further from the coastline and therefore, experiences a greater fetch, which is the distance over which waves propagate under the sustained influence of wind without interruption (Massel, 2013). Longer fetch can increase wave energy at lower frequencies (Webb, 1998); however, prevailing winds are not from the east, such that increased fetch at HYSB1 likely doesn't fully account for the observed difference. Certain water depths can also promote microseismic energy at given frequencies (Kedar et al., 2008; Longuet-Higgins, 1950); although we consider a wide frequency band that extends well above where microseisms dominate noise, this depth-dependent interaction could contribute to the differences seen between Slope Base (2920 m depth) and Hydrate Ridge (790 m depth). The Hydrate Ridge site is also situated much closer in depth to the SOFAR channel (~650 m in the Northeast Pacific; Wagstaff, 2005), which acts as a waveguide for sound in the ocean and allows signals

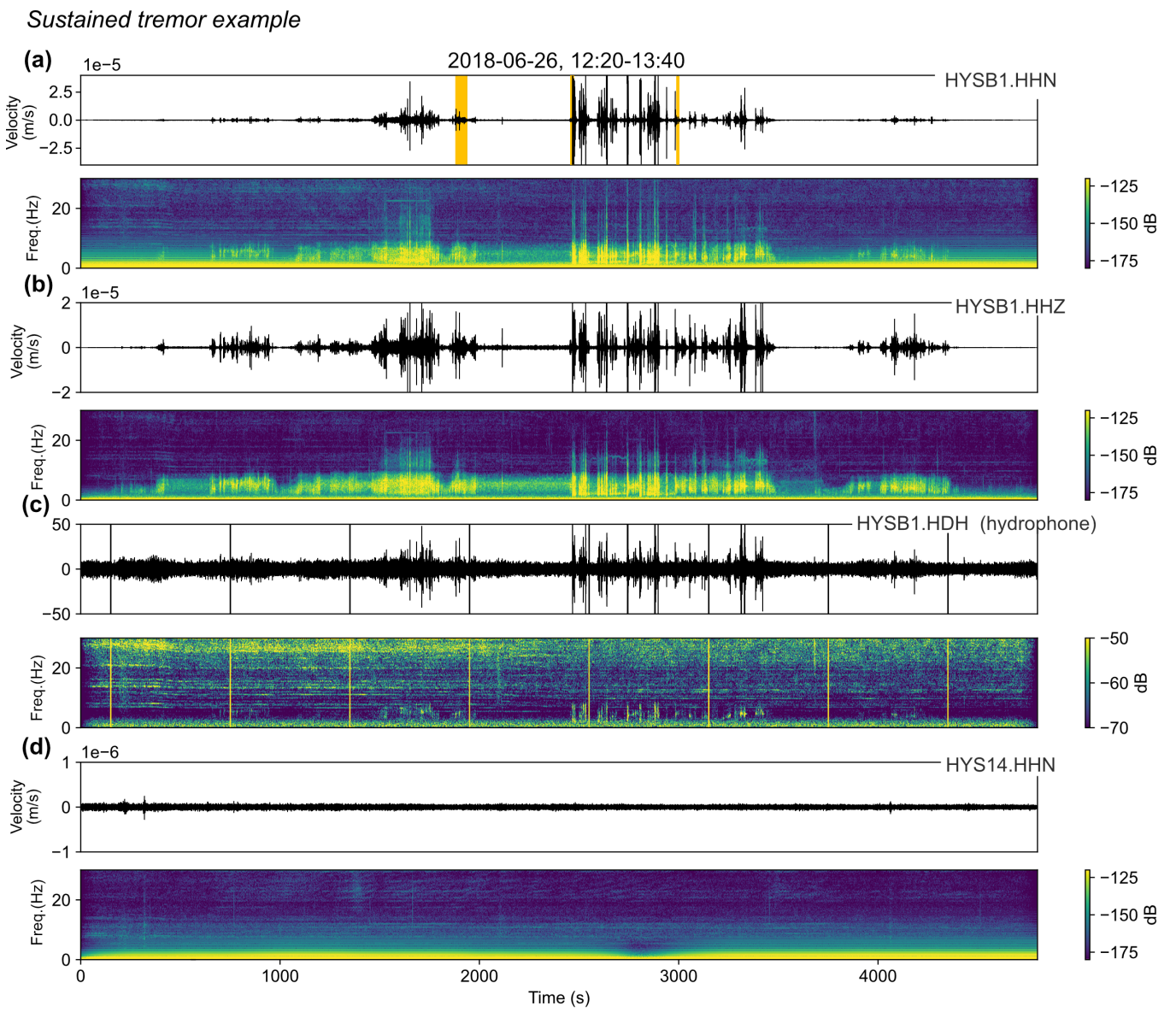

Figure 7 Full 70-minute period for one example of sustained tremor at Slope Base shown for multiple channels and at Hydrate Ridge. All waveforms are filtered from 3-10 Hz. Waveforms in a-c are clipped to focus on the tremor-like signal. Start and end time of the window is noted atop (a). **(a)** Waveform and spectrogram of the Slope Base horizontal channel. On the waveform plot, yellow rectangles denote time windows of our STA/LTA detections (Figure 6a). **(b)** Same as (a) but for the vertical channel. **(c)** Same as (a) but for the hydrophone channel. Note that impulsive broadband signals that recur every 15 minutes are instrument glitches. **(d)** Same as (a) but for the Hydrate Ridge horizontal channel.

to travel over long distances; this leads to higher background noise levels at Hydrate Ridge in comparison to Slope Base (Ragland et al., 2022). This influence of distant noise sources at Hydrate Ridge could diminish the observed relationship between seismic noise and other factors.

5.2 Non-tectonic explanations for Slope Base tremor

The tectonic tremor-like signals recorded at Slope Base (station HYSB1), which occur several times as hour-long episodes and other times as isolated bursts (Figure 6), are the first reported offshore Cascadia. However, it is not possible to validate these detections as tectonic tremor without recording them on multiple instruments and associating them to a feasible source. In this section, we explore several potential non-tectonic sources for the observed signals.

We can rule out the possibility that these signals are related to bottom currents because the instrument is buried, the timing does not correlate with increased in situ measured bottom currents, and the signals do not display the gliding spectral banding expected for bottom current-induced tremor (Essing et al., 2021; Corela et al., 2023). During one of the sustained periods of tremor-like signals, there are some gliding spectral characteristics, but these occur only during the strongest signals and are not observed during the other sustained tremor periods (Figure S10) or during isolated bursts of tremor (Figure S11). The gliding spectra could be a resonant response of the instrument to ground shaking.

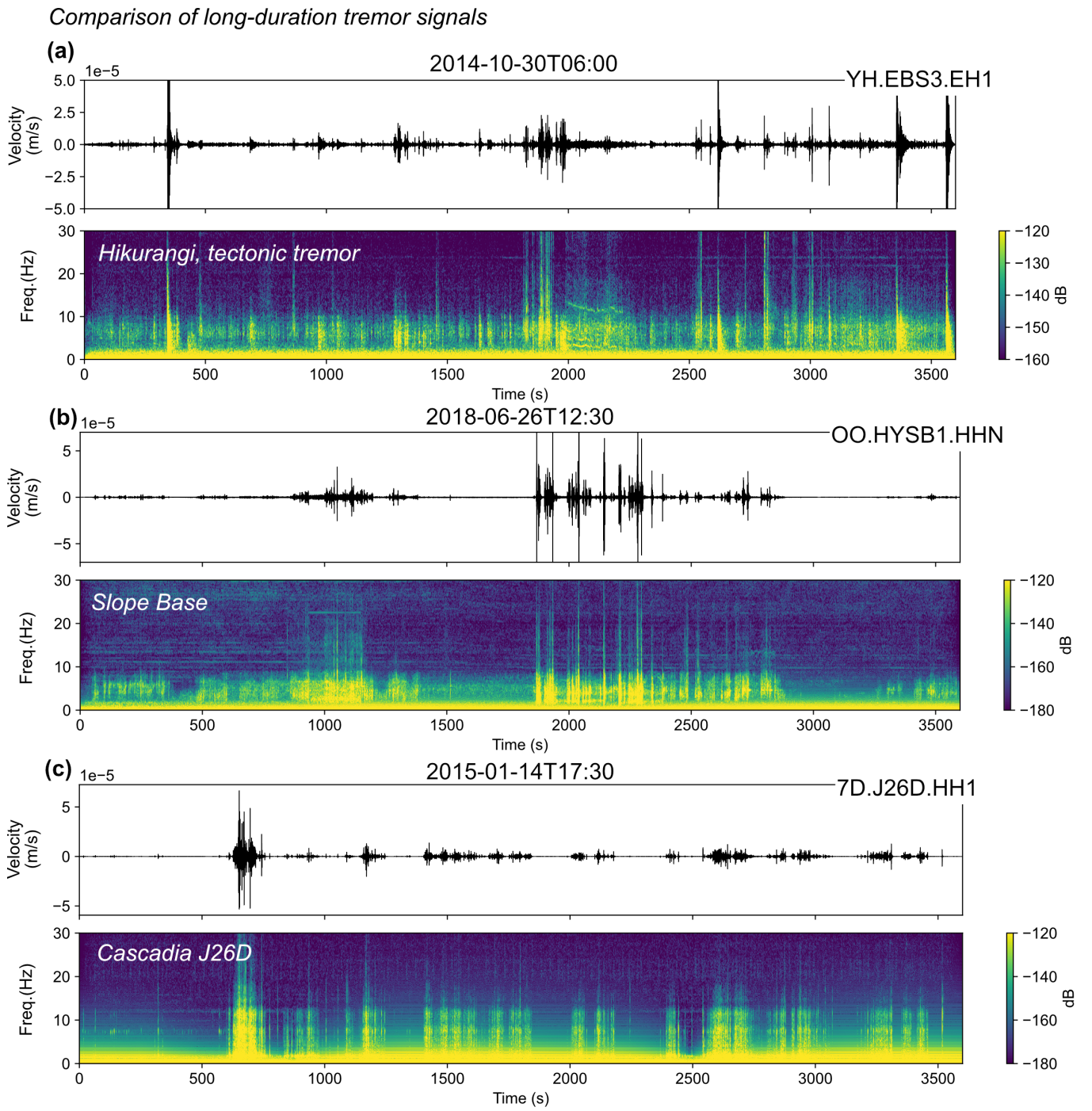

Figure 8 Comparison of 1 hour of tremor-like signals measured on three different instruments: **(a)** Confirmed, located tectonic tremor recorded at Hikurangi by instrument EBS3 (Figure 4a), **(b)** sustained tremor-like signal from our detections at Slope Base, **(c)** similar sustained tremor-like signal at autonomous Cascadia Initiative instrument J26D (Figure 1), found via preliminary application of our approach. In all subplots, the 3-10 Hz waveform and spectrogram are shown for the horizontal channels. The full instrument code, comprising network, station, and channel, and the start time of the window, are labelled atop each subplot.

Because they are only seen on station HYSB1, it is possible that the tremor-like signals are related to instrument noise. To investigate whether the tremor-like signals are recorded by a different similarly-situated instrument , we applied our approach to a nearby OBS from the autonomous Cascadia Initiative experiment that overlapped with the beginning of the HYSB1 recording period (January 2015-July 2015). The autonomous instrument (network code 7D, station code J26D) is located on the incoming plate, ~15 km north of HYSB1 and, similarly, 6 km west of the deformation front (Figure 1b). We do not present full findings for the J26D station because the instrument is unburied and therefore plagued by bottom current-generated tremor (Section 5.1), but we do report at least one sustained tremor-like signal in January 2015 (Figure 8c). This signal is similar in both waveform and spectral characteristics to the tremor-like signals on HYSB1, apart from

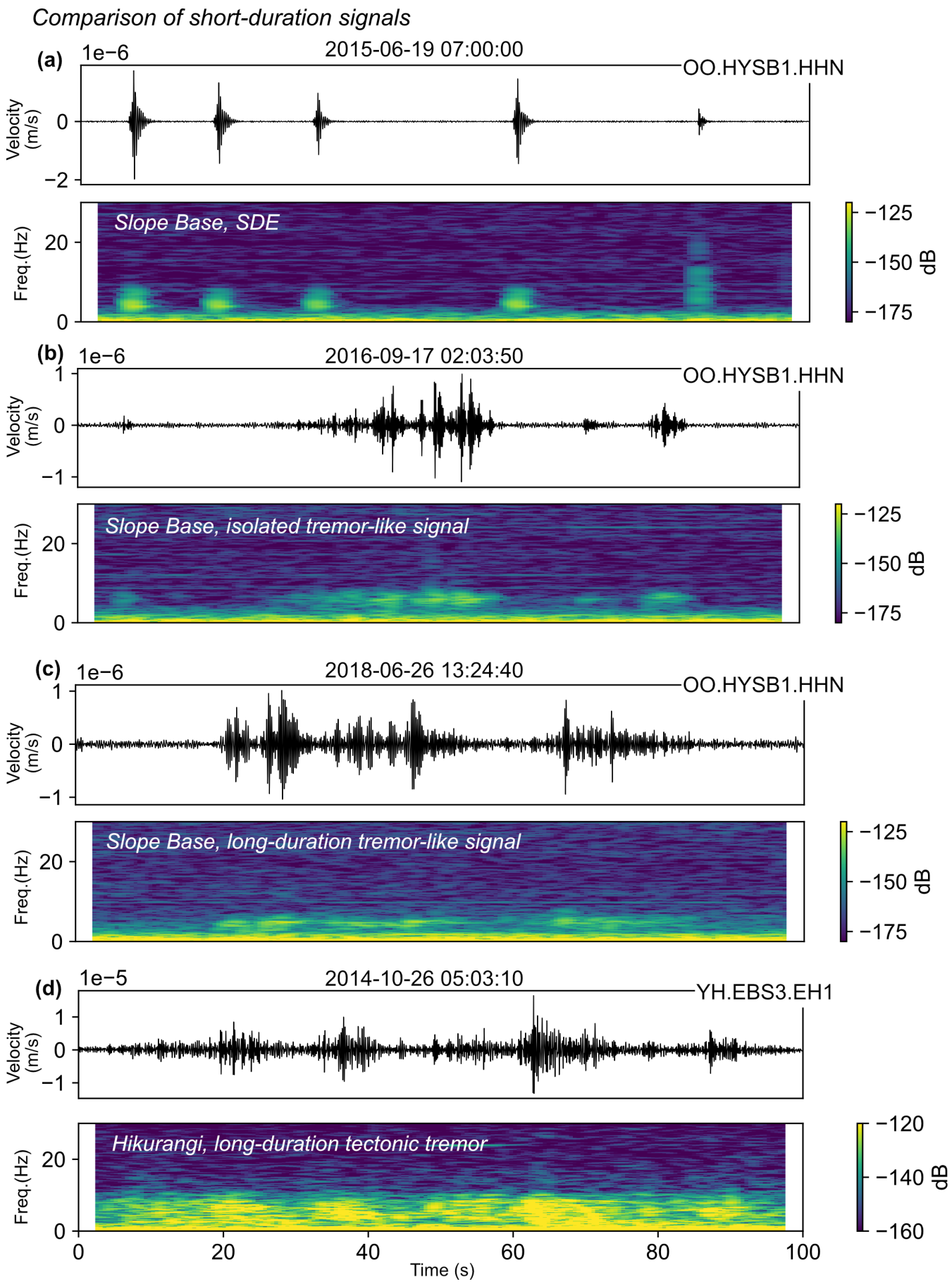

Figure 9 Zoomed-in comparison of 100 seconds of signals: **(a)** short duration events (SDEs) detected at Slope Base, **(b)** an isolated tremor-like signal recorded at Slope Base, **(c)** a snippet of a longer sustained tremor-like signal at Slope Base, **(d)** a snippet from a longer sustained confirmed tectonic tremor period at Hikurangi. Figure format follows Figure 8, with all waveforms filtered from 3-10 Hz.

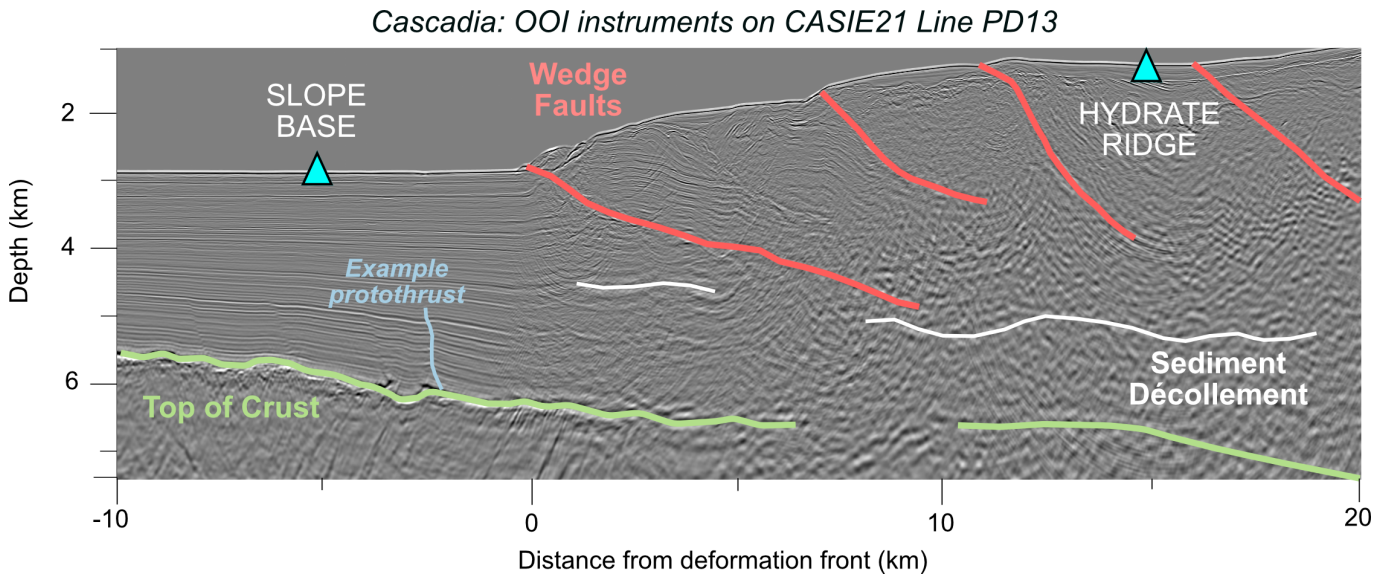

Figure 10 Subsurface structure across-strike near the OOI instruments, shown by processed pre-stack depth-migrated seismic reflection data from Line PD13 of the CASIE21 survey (Figure 1b; Canales et al., 2023). Top of crust, sediment décollement, and wedge fault interpretations are from Carbotte et al. (2024). A clear protothrust on the incoming plate is also interpreted. Note the ~2x vertical exaggeration. The location of the Slope Base and Hydrate Ridge OBSs are shown using cyan triangles, demonstrating that if tectonic tremor occurs near the deformation front, it is ~15 km from Hydrate Ridge and only ~5 km from Slope Base.

a slightly higher maximum frequency (Figure 8). The similarities between these signals suggests they are not internally generated instrument noise, because they are recorded on two different sensor types: both a buried Guralp CMG-1T sensor (HYSB1) and an unburied Nanometrics Trillium sensor in Lamont housing (J26D). However, the signals are never contemporaneously recorded at both stations during their 6-month overlap period. This suggests that the signal source is near each station.

Our tremor-like signals are distinct from SDEs (Figure 9), but at several other seafloor locations, gas- or fluid-induced SDEs have been shown to occur alongside tremor-like signals (Díaz et al., 2007; Hsu et al., 2013; Tsang-Hin-Sun et al., 2018). Similarly to our case, these gas-induced tremor-like signals are only recorded at one station at a time and not at all on hydrophones. These signals display similar waveform characteristics to those recorded by HYSB1 at Slope Base, but differing frequency contents, with either monochromatic (Díaz et al., 2007) or harmonic (Hsu et al., 2013) characteristics or power up to 60 Hz (Tsang-Hin-Sun et al., 2018). We cannot rule out a gas- or fluid-induced mechanism based only on frequency characteristics because they vary from site to site, and it is not unreasonable that gas or fluid migration, or some form of resonance of fluid-filled cracks (Chouet, 1988) could occur near Slope Base. However, we think it is unlikely that our tremor-like signals at Slope Base are gas-induced tremor; there have been extensive observations of gas seeps offshore Cascadia (Merle et al., 2021; Rudebusch et al., 2023), and only several occur near the deformation front, with most concentrated at ~500 m depth. It would also be surprising to see gas-induced tremor at two sites outboard of the deformation front and not at Hydrate Ridge, a known seep site.

Landslides are another potential tremor source; the accretionary wedge at ~44.5°N is steep, with ample evidence for slumping activity (e.g., Hill et al., 2022). It is unlikely that the Slope Base tremor signals are a result of fast-moving landslides, which typically exhibit single-pulse emergent signals with frequencies much higher than 10 Hz (La Rocca et al., 2004; Provost et al., 2018; Schöpa et al., 2018) and are strongly recorded on hydrophones in the marine setting (e.g., Caplan-Auerbach et al., 2014; Chadwick et al., 2011). However, a slow-moving landslide or slumping process cannot be ruled out; slow-moving landslides can exhibit a variety of tremor-like signals that are typically > 10 Hz, but this can vary across sites (Gomberg et al., 2011; Vouillamoz et al., 2018).

5.3 Tectonic explanations for Slope Base tremor

Our reported tremor-like signals at Slope Base, in both waveform envelope and frequency, are consistent with the tectonic tremor signals observed at Hikurangi (see Figures 8 and 9), so we consider potential tectonic sources. Although subducted seamounts are present beneath the Cascadia forearc due east of our study area (Figure 1; Carbotte et al., 2024; Morton et al., 2018, 2023; Tréhu et al., 2012; Williams et al., 2011), seamount-associated deformation is an unlikely tectonic source for our observations because we only record tectonic tremor-like signals at Slope Base, which is further from the seamounts than Hydrate Ridge (~75 km).

Structures closer to Slope Base that may generate tectonic tremor include protothrusts or bending faults on the incoming plate, nearby strike-slip faults, wedge faults, and the décollement. Near Slope Base on the incoming plate, multi-channel seismic imaging has shown that high pore fluid pressures occur on pro-

tothrusts and an incipient décollement in a zone that extends 6 km seaward of the deformation front (Cochrane et al., 1994; Moore et al., 1995); bending faults also occur within 10 km of the deformation front (Han et al., 2016). Also, less than 10 km north of Slope Base, the Alvin Canyon strike-slip fault, which has been inferred to be a drainage pathway for fluid overpressures (Philip et al., 2023), intersects the deformation front (Goldfinger et al., 1997). There are also significant wedge faults near the OOI stations that extend to the décollement (Figure 10; Carbotte et al., 2024), and brittle structures within folds on the accretionary wedge could generate microearthquakes and potentially tremor-like signals within larger stable slip (e.g., Remitti et al., 2024). Indeed, a similar mix of deformational structures, including an incipient décollement and a frontal thrust within the outermost accretionary wedge, has recently been tied to tectonic tremor in Nankai that occurs near the toe of the accretionary wedge and beyond the trench (Kimura et al., 2024; Ogiso and Tamaribuchi, 2022; Tamaribuchi et al., 2022).

It is also possible that slow slip occurs across a larger portion of the plate interface that includes Hydrate Ridge, but tremor is only generated nearer to the deformation front; a similar scenario has been seen in the Nankai subduction zone (Araki et al., 2017). Slow slip on the very shallow plate interface would not necessarily contradict existing findings of a locked megathrust: although existing models for Cascadia suggest shallow locking (Li et al., 2018), on-land data can be fit with or without slip right at the trench. Localized shallow slow slip could also be consistent with preliminary GNSS-A datasets that suggest full locking (DeSanto et al., 2025); in Nankai, long-term seafloor GNSS-A measurements (Yokota et al., 2016) suggest full locking even in the same regions slow slip transients are observed (Araki et al., 2017).

Several of the sustained tremor periods at HYSB1 contain spiky broadband signals that are not seen in deep downdip tremor in Cascadia (Figures 7-8 and S8). However, spikiness within tectonic tremor signals is also seen in other regions including Guerrero and Japan (Husker et al., 2019; Ito et al., 2015), and impulsive arrivals embedded within tectonic tremor in Japan and Alaska can lead to a spikier appearance than in deep Cascadia (see Figures 1 and 2 Schwartz and Rokosky, 2007; Ide, 2010, see their Figure 4). If the signals at HYSB1 are indeed tectonic tremor occurring at very shallow depths, they may appear spikier than their downdip counterparts due to a lack of attenuation. Indeed, approximating attenuation via Azimi's relation (Azimi, 1968), assuming the depth of downdip Cascadia tremor, slightly dulls the spikiness of our tremor signals and improves the relative amplitude of the emergent portions of the waveform (Figure S12).

Waveform similarity and consistent polarization of the tremor signals at HYSB1 throughout time suggest a consistent source area. If the signals are indeed tectonic tremor, they could be thought of as the sum of many low frequency earthquakes (LFEs) (Shelly et al., 2007). We cannot identify LFEs within tremor using a single station, but if the signals at HYSB1 are composed of many LFEs emanating from the same area, we might expect to see similar waveforms at the time scales of LFEs repeating over time (~6 s windows; Brown et al., 2008). Indeed, if our tremor signals are split into 6-s templates, they contain many examples of templates that have high similarity to other portions of tremor signals, years apart (see Figure S13). Further, if we examine the three-component particle motion of these 6-s templates (Flinn, 1965), we find that many have a high degree of rectilinearity and show consistent particle motions over time (see Figure S14). Similar rectilinearity values are seen for the signal recorded at station J26D (Figure 8c). These stable polarization characteristics are consistent with a tectonic tremor source (e.g., Bostock and Christensen, 2012; Iwasaki et al., 2022). With data from a single station, however, we cannot use these particle motions to identify a specific tremor source location; particle motions of tectonic tremor are a result of complex S-wave radiation patterns, local anisotropy, and faulting mechanisms, which means distinct tremor sources could produce equivalent particle motions at a single receiver.

Based on timing, it is unlikely that the tectonic tremor-like signals observed at Slope Base are triggered either by large earthquakes or downdip slow slip. Dynamically triggered tectonic tremor occurring within the passing surface waves of large earthquakes has been extensively observed in deep Cascadia (e.g., Gomberg, 2010; Rubinstein et al., 2007). However, the shortest time between a preceding global M7+ earthquake and an HYSB1 tremor detection is ~9 hours. To check whether there is dynamically triggered tremor recorded at HYSB1 that our detection approach missed, we manually examined the surface wave arrivals of the nearest large earthquakes (Figure S15). We found that even the largest surface waves do not appear to modulate the waveform at tremor frequencies, as is expected for triggered tremor. We note that that dynamically triggered tremor is not necessarily expected for a given tremor source; triggered tremor is more likely to be observed when a tremor patch is currently active, or more highly stressed than normal (Rubinstein et al., 2009a; Gomberg, 2010).

We also see no clear timing relationship between the HYSB1 tremor detections and episodes of deep tectonic tremor at similar latitudes (Wech, 2010). Observed triggering relationships between deep downdip and shallow updip slow slip at subduction zones are few, but have been noted at Nankai and Costa Rica at time scales from instantaneous to several weeks (Davis et al., 2015; Hirose et al., 2010). In 2016 and 2017, sustained tremor episodes at HYSB1 occur ~6 months after downdip tremor at similar latitudes, but in 2015 and 2018, no downdip tremor precedes sustained tremor periods (Figure 6b).

5.4 Impacts of site location on tremor detection sensitivity

The Hydrate Ridge station does not record the same tectonic tremor-like signals we see at Slope Base (Figures 7 and S9), although it is only 20 km further landward (Fig-

ure 1). Although this is likely because the tremor source is localized and much closer to Slope Base, here we also explore how site location may play a role in the recording sensitivity of tectonic tremor.

The Hydrate Ridge station records many more emergent signals overall in comparison to Slope Base (Figure 5). However, this is likely only due to the closer proximity of Hydrate Ridge to the SOFAR channel, which allows many more T-phases to be recorded (Okal, 2008; Hamada, 1985). Indeed, visual inspection of the Hydrate Ridge detections shows that there are many more T-phases recorded than we discard with our method (Text S1 and Figure S9). Many of these can be identified as "slope" type T-phases, which have multiple peaks and frequencies primarily < 10 Hz (Johnson et al., 1967; Walker et al., 1992; de Groot-Hedlin and Orcutt, 2001). Although SOFAR channel proximity clearly increases the overall number of emergent signals recorded on the Hydrate Ridge station, we would not expect it to improve sensitivity to tectonic tremor signals, which do not travel in the water column.

To consider how sensitive tectonic tremor measurement can be to distance, we can consider the Hikurangi OBS tectonic tremor dataset (Figure 4). Figure 11 shows the relationship between station-to-tremor distance and maximum ground velocity amplitudes in 300 s windows reported for five different tremors located by Todd et al. (2018). Although there is some variability, overall, it appears that the amplitude of tectonic tremor signals diminishes by one order of magnitude between recordings made at ~5 km from the source versus those made at ~40 km. Our single-station detection method also shows much better timing agreement with the Todd et al. (2018) tremor catalog when the tremor source is < 40 km from the station, with the best agreement observed at distances of < 20 km (Figure 4e-f).

There is also evidence from some other subduction zones of channeling of tremor signals that varies based on relative location of the source to the plate interface. At Hikurangi, the tectonic tremor source is inferred to be at 5-10 km depth on the plate interface (Todd et al., 2018). While tectonic tremor is recorded at two sites on the overriding plate, both directly atop it (EBS3) and at a site ~30-40 km away (EBS5), it is not simultaneously recorded at a site also ~30-40 km away on the incoming plate (LOBS2) (Figure 4). We note that the LOBS2 seismometer type differs from the EBS3 and EBS5 stations. However, we visually checked recordings from the same seismometer type (LOBS5) on the overriding plate and found that it recorded tectonic tremor while LOBS2, on the incoming plate, did not.

Contrastingly, in Nankai, the tectonic tremor source is inferred to be at < 5 km depth on the plate interface, and the signal appears more clearly on stations near the deformation front. Araki et al. (2017) show that tremor occurring near the trench has the highest amplitudes on buried OBSs < 5-10 km landward of the trench; ~20-30 km landward, the tremor is still recorded by some buried OBSs, but is quieter overall and is nearly indiscernible on some stations (see their Figure S2). Although the signal type is different, Nakano et al. (2018) also report nearby very low frequency earthquakes that

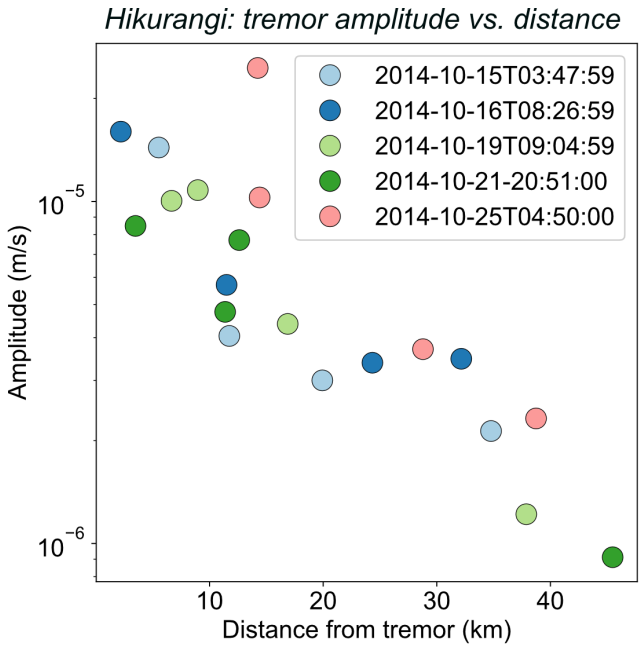

Figure 11 Scatter plot showing maximum amplitudes associated with the 3-10 Hz filtered waveform at 4 different stations at varying distances from tremor (EBS2, EBS3, EBS4, and EBS5; see Figure 4a). Points are colored by the tremor time they pertain to; 5 different tremor examples are shown. We visually checked each of the seismometers to confirm that they were recording tectonic tremor and not a different signal. We do not show amplitudes for stations whose codes begin with LOBS because the reported station response yielded unreasonable velocity values.

are also most strongly recorded near the trench, with diminished amplitudes on stations 20-30 km landward (see their Figure 2). Taken alongside the contrasting deeper example from Hikurangi, these observations support the idea that a localized tectonic tremor signal occurring at < 5 km depths could be recorded at one station on the incoming plate and not at another station ~20 km away on the overriding plate, as is our case (Figure 10).

6 Conclusions

We have developed a technique to isolate tectonic tremor-like signals on a single OBS amidst the presence of T-phases and ship noise. We demonstrate the efficacy of this technique through comparison to a multi-station tectonic tremor catalog for OBSs in the offshore Hikurangi subduction zone, and we show that our technique does not spuriously detect nonexistent tremor on an additional OBS dataset in the central Pacific. This approach could potentially be adapted elsewhere to identify tectonic tremor in OBS datasets where station spacing is large and/or T-phases are dominant. However, using unburied instruments would require further work to identify and discard signals of harmonic bottom current-generated tremor. To handle these additional noise signals or process larger datasets, machine learning techniques (e.g., Holtzman et al., 2018; Seydoux et al., 2020) could first identify and cluster similar

emergent signals, and then our straightforward waveform and spectra analyses could be applied to help identify tectonic tremor-like signals within clustering results.

We apply our single-station tectonic tremor detection to two long-term cabled OBSs deployed in the Cascadia subduction zone at ~44.5°N. We show that the burial of these instruments prevents harmonic bottom current-generated tremor and likely weakens the overall relationship between bottom currents and seismic noise. We identify tectonic tremor-like signals at the Slope Base HYSB1 station on the incoming plate, ~5 km seaward of the deformation front, that recur throughout February 2015-January 2024. These same signals are not recorded at the Hydrate Ridge HYS14 station, ~15 km landward of the deformation front. We cannot easily attribute the Slope Base tremor-like signals to instrumental, bottom current, or gas-induced noise, and we show that they are largely consistent with the characteristics expected for tectonic tremor. Tectonic tremor sources near Slope Base could include protothrusts or bending faults on the incoming plate, nearby strike-slip faults including the Alvin Canyon Fault, faulting in the outer accretionary wedge, or localized slow slip on the shallow portion of the plate interface. With observation on only one station, we cannot conclude whether the signals are tectonic tremor from a localized source very near Slope Base, or another signal altogether, such as a slow-moving landslide process in the outermost wedge.

Additional observations are needed to rule out potential signal sources and explore whether tremor-like signals occur near the deformation front elsewhere in Cascadia. Application of our single-station tectonic tremor detection technique to more sites from the autonomous Cascadia Initiative experiment could explore whether the tremor-like signals we observe at Slope Base are widespread or spatially concentrated. The planned deployment of four additional cabled OBSs to the OOI observatory through the COSZO project will also provide further opportunity to expand observations of potential tectonic tremor-like signals and may allow the identification of LFEs (e.g., Brown et al., 2008). Seafloor geodetic techniques that can measure small fault slip transients, including fiber optic strainmeters, borehole strainmeters (Johnston and Linde, 2002), and seafloor pressure sensing (e.g., Woods et al., 2024) would also be useful to determine whether tremor-like signals are tectonic in origin.

Acknowledgements

We thank Anna Ledeczi, Harold Tobin, Joan Gomberg, Maleen Kidiwela, Marine Denolle, and Aaron Wech for helpful conversations that improved the manuscript. We also thank Anne Tréhu and an anonymous reviewer for helpful reviews that greatly strengthened the manuscript. Partial funding support was provided by the Jerome M. Paros Endowed Chair in Sensor Networks and by a National Defense Science and Engineering Graduate Fellowship to ZK.

7 Data and code availability

All seismic waveform data used in this study are publicly available through IRIS Web Services (https://service.iris.edu/). IRIS Data Services are funded through the Seismological Facilities for the Advancement of Geoscience (SAGE) Award of the National Science Foundation under Cooperative Support Agreement EAR-1851048. Seismic networks used in this study include the Ocean Observatories Initiative network (network code OO; NSF Ocean Observatories Initiative, 2013), the HOBITSS network (network code YH; Wallace et al., 2014), the NoMelt Experiment (network code ZA; Lin et al., 2016) and the Cascadia Initiative Community Experiment (network code 7D; IRIS OBSIP, 2011). All other datasets used in this study, including tremor datasets, bottom current time series, and wind speeds, are open-source and have been cited where applicable. The Python codes used to implement the approach and produce the results presented here can be found at the following Github repository: https://github.com/zoekrauss/obs_tremor, stored on Zenodo (Krauss, 2024).

8 Competing interests

The authors have no competing interests.

References

Andrew, R. K., Howe, B. M., and Mercer, J. A. Long-time trends in ship traffic noise for four sites off the North American West Coast. *The Journal of the Acoustical Society of America*, 129(2): 642–651, Feb. 2011. doi: 10.1121/1.3518770.

Annoura, S., Hashimoto, T., Kamaya, N., and Katsumata, A. Shallow episodic tremor near the Nankai Trough axis off southeast Mie prefecture, Japan. *Geophysical Research Letters*, 44(8): 3564–3571, Apr. 2017. doi: 10.1002/2017gl073006.

Araki, E., Saffer, D. M., Kopf, A. J., Wallace, L. M., Kimura, T., Machida, Y., Ide, S., Davis, E., Toczko, S., Carr, S., Kinoshita, C., Kobayashi, R., and Rösner, A. Recurring and triggered slow-slip events near the trench at the Nankai Trough subduction megathrust. *Science*, 356(6343):1157–1160, June 2017. doi: 10.1126/science.aan3120.

Azimi, A. Impulse and transient characteristics of media with linear and quadratic absorption laws, Izvestiya. *Phys. of the Solid Earth*, 0:88–93, 1968.

Barcheck, G., Abers, G. A., Adams, A. N., Bécel, A., Collins, J., Gaherty, J. B., Haeussler, P. J., Li, Z., Moore, G., Onyango, E., Roland, E., Sampson, D. E., Schwartz, S. Y., Sheehan, A. F., Shillington, D. J., Shore, P. J., Webb, S., Wiens, D. A., and Worthington, L. L. The Alaska Amphibious Community Seismic Experiment. *Seismological Research Letters*, 91(6):3054–3063, Aug. 2020. doi: 10.1785/0220200189.

Batsi, E., Tsang-Hin-Sun, E., Klingelhoefer, F., Bayrakci, G., Chang, E. T., Lin, J., Dellong, D., Monteil, C., and Géli, L. Nonseismic Signals in the Ocean: Indicators of Deep Sea and Seafloor Processes on Ocean-Bottom Seismometer Data. *Geochemistry, Geophysics, Geosystems*, 20(8):3882–3900, Aug. 2019. doi: 10.1029/2019gc008349.

Beroza, G. C. and Ide, S. Slow Earthquakes and Nonvolcanic Tremor. *Annual Review of Earth and Planetary Sciences*, 39 (1):271–296, May 2011. doi: 10.1146/annurev-earth-040809-152531.

Borghi, A., Aoudia, A., Javed, F., and Barzaghi, R. Precursory slow-slip loaded the 2009 L'Aquila earthquake sequence. *Geophysical Journal International*, 205(2):776–784, Jan. 2016. doi: 10.1093/gji/ggw046.

Bostock, M. G. and Christensen, N. I. Split from slip and schist: Crustal anisotropy beneath northern Cascadia from non-volcanic tremor. *Journal of Geophysical Research: Solid Earth*, 117(B8), Aug. 2012. doi: 10.1029/2011jb009095.

Brown, J. R., Beroza, G. C., and Shelly, D. R. An autocorrelation method to detect low frequency earthquakes within tremor. *Geophysical Research Letters*, 35(16), Aug. 2008. doi: 10.1029/2008gl034560.

Brudzinski, M. R. and Allen, R. M. Segmentation in episodic tremor and slip all along Cascadia. *Geology*, 35(10):907, 2007. doi: 10.1130/g23740a.1.

Burgette, R. J., Weldon, R. J., and Schmidt, D. A. Interseismic uplift rates for western Oregon and along-strike variation in locking on the Cascadia subduction zone. *Journal of Geophysical Research: Solid Earth*, 114(B1), Jan. 2009. doi: 10.1029/2008jb005679.

Buskirk, R. E., Frohlich, C., Latham, G. V., Chen, A. T., and Lawton, J. Evidence that biological activity affects Ocean Bottom Seismograph recordings. *Marine Geophysical Researches*, 5(2):189–205, June 1981. doi: 10.1007/bf00163479.

Bürgmann, R. The geophysics, geology and mechanics of slow fault slip. *Earth and Planetary Science Letters*, 495:112–134, Aug. 2018. doi: 10.1016/j.epsl.2018.04.062.

Canales, J. P., Miller, N. C., Baldwin, W., Carbotte, S. M., Han, S., Boston, B., Jian, H., Collins, J., and Lizarralde, D. CASIE21-OBS: An Open-Access, OBS Controlled-Source Seismic Data Set for Investigating the Structure and Properties of the Cascadia Accretionary Wedge and the Downgoing Explorer-Juan de Fuca-Gorda Plate System. *Seismological Research Letters*, May 2023. doi: 10.1785/0220230010.

Caplan-Auerbach, J., Dziak, R. P., Bohnenstiehl, D. R., Chadwick, W. W., and Lau, T. Hydroacoustic investigation of submarine landslides at West Mata volcano, Lau Basin. *Geophysical Research Letters*, 41(16):5927–5934, Aug. 2014. doi: 10.1002/2014gl060964.

Carbotte, S. M., Boston, B., Han, S., Shuck, B., Beeson, J., Canales, J. P., Tobin, H., Miller, N., Nedimovic, M., Tréhu, A., Lee, M., Lucas, M. C., Jian, H., Jiang, D., Moser, L., Anderson, C., Judd, D., Fernandez, J., Campbell, C., Goswami, A., and Gahlawat, R. Subducting plate structure and megathrust morphology from deep seismic imaging linked to earthquake rupture segmentation at Cascadia. *Science Advances*, 10(23), June 2024. doi: 10.1126/sciadv.adl3198.

Carvajal, M., Sun, T., Wang, K., Luo, H., and Zhu, Y. Evaluating the Tsunamigenic Potential of Buried Versus Trench-Breaching Megathrust Slip. *Journal of Geophysical Research: Solid Earth*, 127(8), Aug. 2022. doi: 10.1029/2021jb023722.

Chadwick, W. W., Dziak, R. P., Haxel, J. H., Embley, R. W., and Matsumoto, H. Submarine landslide triggered by volcanic eruption recorded by in situ hydrophone. *Geology*, 40(1):51–54, Nov. 2011. doi: 10.1130/g32495.1.

Chaudhuri, K. and Ghosh, A. Widespread Very Low Frequency Earthquakes (VLFEs) Activity Offshore Cascadia. *Geophysical Research Letters*, 49(13), July 2022. doi: 10.1029/2022gl097962.

Chouet, B. Resonance of a fluid-driven crack: Radiation properties and implications for the source of long-period events and harmonic tremor. *Journal of Geophysical Research: Solid Earth*, 93 (B5):4375–4400, May 1988. doi: 10.1029/jb093ib05p04375.

Cochrane, G. R., Moore, J. C., MacKay, M. E., and Moore, G. F. Velocity and inferred porosity model of the Oregon accretionary prism from multichannel seismic reflection data: Implications on sediment dewatering and overpressure. *Journal of Geophysical Research: Solid Earth*, 99(B4):7033–7043, Apr. 1994. doi: 10.1029/93jb03206.

Collins, J. A., Vernon, F. L., Orcutt, J. A., Stephen, R. A., Peal, K. R., Wooding, F. B., Spiess, F. N., and Hildebrand, J. A. Broadband seismology in the oceans: Lessons from the Ocean Seismic Network Pilot Experiment. *Geophysical Research Letters*, 28(1): 49–52, Jan. 2001. doi: 10.1029/2000gl011638.

Corela, C., Loureiro, A., Duarte, J. L., Matias, L., Rebelo, T., and Bartolomeu, T. The effect of deep ocean currents on ocean- bottom seismometers records. *Natural Hazards and Earth System Sciences*, 23(4):1433–1451, Apr. 2023. doi: 10.5194/nhess-23-1433-2023.

Curtis, K. R., Howe, B. M., and Mercer, J. A. Low-frequency ambient sound in the North Pacific: Long time series observations. *The Journal of the Acoustical Society of America*, 106(6):3189–3200, Dec. 1999. doi: 10.1121/1.428173.

Dahl, P. H., Dall'Osto, D. R., and Harrington, M. J. Trends in low-frequency underwater noise off the Oregon coast and impacts of COVID-19 pandemic. *The Journal of the Acoustical Society of America*, 149(6):4073–4077, June 2021. doi: 10.1121/10.0005192.

Davis, E. E., Villinger, H., and Sun, T. Slow and delayed deformation and uplift of the outermost subduction prism following ETS and seismogenic slip events beneath Nicoya Peninsula, Costa Rica. *Earth and Planetary Science Letters*, 410:117–127, Jan. 2015. doi: 10.1016/j.epsl.2014.11.015.

De Caro, M., Montuori, C., Frugoni, F., Monna, S., Cammarano, F., and Beranzoli, L. T-Phases Observed at the Ionian Seafloor: Seismic Source and Bathymetric Effects. *Seismological Research Letters*, 92(1):481–493, Sept. 2020. doi: 10.1785/0220200096.

de Groot-Hedlin, C. D. and Orcutt, J. A. Excitation of T-phases by seafloor scattering. *The Journal of the Acoustical Society of America*, 109(5):1944–1954, May 2001. doi: 10.1121/1.1361057.

DeSanto, J. B., Schmidt, D. A., Zumberge, M., Sasagawa, G., and Chadwell, C. D. Near full locking on the shallow megathrust of the central Cascadia subduction zone revealed by GNSS-Acoustic. *Earth and Planetary Science Letters*, 665:119463, Sept. 2025. doi: 10.1016/j.epsl.2025.119463.

Duennebier, F. K. and Sutton, G. H. Why bury ocean bottom seismometers? *Geochemistry, Geophysics, Geosystems*, 8(2), Feb. 2007. doi: 10.1029/2006gc001428.

Dziak, R., Hammond, S., and Fox, C. A 20-Year Hydroacoustic Time Series of Seismic and Volcanic Events in the Northeast Pacific Ocean. *Oceanography*, 24(3):280–293, Sept. 2011. doi: 10.5670/oceanog.2011.79.

Díaz, J., Gallart, J., and Gaspà, O. Atypical seismic signals at the Galicia Margin, North Atlantic Ocean, related to the resonance of subsurface fluid-filled cracks. *Tectonophysics*, 433(1–4):1–13, Apr. 2007. doi: 10.1016/j.tecto.2007.01.004.

Essing, D., Schlindwein, V., Schmidt-Aursch, M. C., Hadziioannou, C., and Stähler, S. C. Characteristics of Current-Induced Harmonic Tremor Signals in Ocean-Bottom Seismometer Records. *Seismological Research Letters*, 92(5):3100–3112, Apr. 2021. doi: 10.1785/0220200397.

Flinn, E. Signal analysis using rectilinearity and direction of particle motion. *Proceedings of the IEEE*, 53(12):1874–1876, 1965. doi: 10.1109/proc.1965.4462.

Goldfinger, C., Kulm, L. D., Yeats, R. S., McNeill, L., and Hummon, C. Oblique strike-slip faulting of the central Cascadia submarine forearc. *Journal of Geophysical Research: Solid Earth*, 102(B4): 8217–8243, Apr. 1997. doi: 10.1029/96jb02655.

Gomberg, J. Lessons from (triggered) tremor. *Journal of Geophysical Research: Solid Earth*, 115(B10), Oct. 2010. doi: 10.1029/2009jb007011.

Gomberg, J., Schulz, W., Bodin, P., and Kean, J. Seismic and geodetic signatures of fault slip at the Slumgullion Landslide Natural Laboratory. *Journal of Geophysical Research*, 116(B9), Sept. 2011. doi: 10.1029/2011jb008304.

Hamada, N. T waves recorded by ocean bottom seismographs off the south coast of Tokai area, central Honshu, Japan. *Journal of Physics of the Earth*, 33(5):391–410, 1985. doi: 10.4294/jpe1952.33.391.

Han, S., Carbotte, S. M., Canales, J. P., Nedimović, M. R., Carton, H., Gibson, J. C., and Horning, G. W. Seismic reflection imaging of the Juan de Fuca plate from ridge to trench: New constraints on the distribution of faulting and evolution of the crust prior to subduction. *Journal of Geophysical Research: Solid Earth*, 121 (3):1849–1872, Mar. 2016. doi: 10.1002/2015jb012416.

Hanson, J. A. and Bowman, J. R. Methods for monitoring hydroacoustic events using direct and reflected T waves in the Indian Ocean. *Journal of Geophysical Research: Solid Earth*, 111(B2), Feb. 2006. doi: 10.1029/2004jb003609.

Hayes, G. P., Moore, G. L., Portner, D. E., Hearne, M., Flamme, H., Furtney, M., and Smoczyk, G. M. Slab2, a comprehensive subduction zone geometry model. *Science*, 362(6410):58–61, Oct. 2018. doi: 10.1126/science.aat4723.

Hersbach, H., Bell, B., Berrisford, P., Hirahara, S., Horányi, A., Muñoz-Sabater, J., Nicolas, J., Peubey, C., Radu, R., Schepers, D., Simmons, A., Soci, C., Abdalla, S., Abellan, X., Balsamo, G., Bechtold, P., Biavati, G., Bidlot, J., Bonavita, M., De Chiara, G., Dahlgren, P., Dee, D., Diamantakis, M., Dragani, R., Flemming, J., Forbes, R., Fuentes, M., Geer, A., Haimberger, L., Healy, S., Hogan, R. J., Hólm, E., Janisková, M., Keeley, S., Laloyaux, P., Lopez, P., Lupu, C., Radnoti, G., de Rosnay, P., Rozum, I., Vamborg, F., Villaume, S., and Thépaut, J. The ERA5 global reanalysis. *Quarterly Journal of the Royal Meteorological Society*, 146 (730):1999–2049, June 2020. doi: 10.1002/qj.3803.

Hill, J. C., Watt, J. T., and Brothers, D. S. Mass wasting along the Cascadia subduction zone: Implications for abyssal turbidite sources and the earthquake record. *Earth and Planetary Science Letters*, 597:117797, Nov. 2022. doi: 10.1016/j.epsl.2022.117797.

Hilmo, R. and Wilcock, W. S. D. Physical Sources of High-Frequency Seismic Noise on Cascadia Initiative Ocean Bottom Seismometers. *Geochemistry, Geophysics, Geosystems*, 21(10), Oct. 2020. doi: 10.1029/2020gc009085.

Hirose, H., Asano, Y., Obara, K., Kimura, T., Matsuzawa, T., Tanaka, S., and Maeda, T. Slow Earthquakes Linked Along Dip in the Nankai Subduction Zone. *Science*, 330(6010):1502–1502, Dec. 2010. doi: 10.1126/science.1197102.

Holtzman, B. K., Paté, A., Paisley, J., Waldhauser, F., and Repetto, D. Machine learning reveals cyclic changes in seismic source spectra in Geysers geothermal field. *Science Advances*, 4(5), May 2018. doi: 10.1126/sciadv.aao2929.

Hsu, S.-K., Wang, S.-Y., Liao, Y.-C., Yang, T. F., Jan, S., Lin, J.-Y., and Chen, S.-C. Tide-modulated gas emissions and tremors off SW Taiwan. *Earth and Planetary Science Letters*, 369–370:98–107, May 2013. doi: 10.1016/j.epsl.2013.03.013.

Husker, A., Frank, W. B., Gonzalez, G., Avila, L., Kostoglodov, V., and Kazachkina, E. Characteristic Tectonic Tremor Activity Observed Over Multiple Slow Slip Cycles in the Mexican Subduction Zone. *Journal of Geophysical Research: Solid Earth*, 124(1): 599–608, Jan. 2019. doi: 10.1029/2018jb016517.

Ide, S. Quantifying the time function of nonvolcanic tremor based on a stochastic model. *Journal of Geophysical Research: Solid Earth*, 115(B8), Aug. 2010. doi: 10.1029/2009jb000829.

Ide, S. Variety and spatial heterogeneity of tectonic tremor worldwide. *Journal of Geophysical Research: Solid Earth*, 117(B3), Mar. 2012. doi: 10.1029/2011jb008840.

Ide, S., Shelly, D. R., and Beroza, G. C. Mechanism of deep low frequency earthquakes: Further evidence that deep nonvolcanic tremor is generated by shear slip on the plate interface. *Geophysical Research Letters*, 34(3), Feb. 2007. doi: 10.1029/2006gl028890.

IRIS OBSIP. Cascadia Initiative Community Experiment - OBS Component, 2011. doi: 10.7914/SN/7D$_2$011.

Ito, Y., Hino, R., Suzuki, S., and Kaneda, Y. Episodic tremor and slip near the Japan Trench prior to the 2011 Tohoku-Oki earthquake. *Geophysical Research Letters*, 42(6):1725–1731, Mar. 2015. doi: 10.1002/2014gl062986.

Iwasaki, Y., Mochizuki, K., Ishise, M., Todd, E. K., Schwartz, S. Y., Zal, H., Savage, M. K., Henrys, S., Sheehan, A. F., Ito, Y., Wallace, L. M., Webb, S. C., Yamada, T., and Shinohara, M. Continuous Tremor Activity With Stable Polarization Direction Following the 2014 Large Slow Slip Event in the Hikurangi Subduction Margin Offshore New Zealand. *Journal of Geophysical Research: Solid Earth*, 127(2), Feb. 2022. doi: 10.1029/2021jb022161.

Johnson, R. H., Norris, R. A., and Duennebier, F. K. *Abyssally Generated T-phases*. Jan. 1967. doi: 10.21236/ad0649315.

Johnston, M. and Linde, A. *Implications of Crustal Strain During Conventional, Slow, and Silent Earthquakes*, page 589–605. Elsevier, 2002. doi: 10.1016/s0074-6142(02)80239-x.

Kato, A., Obara, K., Igarashi, T., Tsuruoka, H., Nakagawa, S., and Hirata, N. Propagation of Slow Slip Leading Up to the 2011 Mw 9.0 Tohoku-Oki Earthquake. *Science*, 335(6069):705–708, Feb. 2012. doi: 10.1126/science.1215141.

Kedar, S., Longuet-Higgins, M., Webb, F., Graham, N., Clayton, R., and Jones, C. The origin of deep ocean microseisms in the North Atlantic Ocean. *Proceedings of the Royal Society A: Mathematical, Physical and Engineering Sciences*, 464(2091):777–793, Jan. 2008. doi: 10.1098/rspa.2007.0277.

Kelley, D. S., Delaney, J. R., and Team, C. A. NSF's Cabled Array: A wired tectonic plate and overlying ocean. In *OCEANS 2016 MTS/IEEE Monterey*. IEEE, Sept. 2016. doi: 10.1109/oceans.2016.7761398.

Kimura, G., Shiraishi, K., Nakamura, Y., Kodaira, S., Fujie, G., Arai, R., and Moore, G. F. Frontal Thrust Ramp-Up and Slow Earthquakes Due To Underthrusting of Basement High in the Nankai Trough. *Geochemistry, Geophysics, Geosystems*, 25(7), July 2024. doi: 10.1029/2024gc011468.

Krauss, Z., 2024. doi: 10.5281/zenodo.14532861.

La Rocca, M., Galluzzo, D., Saccorotti, G., Tinti, S., Cimini, G. B., and Del Pezzo, E. Seismic Signals Associated with Landslides and with a Tsunami at Stromboli Volcano, Italy. *Bulletin of the Seismological Society of America*, 94(5):1850–1867, 10 2004. doi: 10.1785/012003238.

Lawrence, M. Acoustic monitoring of the global ocean for the CTBT. *Proceedings of ACOUSTICS*, 1:455–460, 2004.

Li, S., Wang, K., Wang, Y., Jiang, Y., and Dosso, S. E. Geodetically Inferred Locking State of the Cascadia Megathrust Based on a Viscoelastic Earth Model. *Journal of Geophysical Research: Solid Earth*, 123(9):8056–8072, Sept. 2018. doi: 10.1029/2018jb015620.

Lin, P.-Y. P., Gaherty, J. B., Jin, G., Collins, J. A., Lizarralde, D., Evans, R. L., and Hirth, G. High-resolution seismic constraints on flow dynamics in the oceanic asthenosphere. *Nature*, 535(7613): 538–541, July 2016. doi: 10.1038/nature18012.

Liu, H. and Tan, Y. J. Automatic Cataloging of Earthquakes in the Northeast Pacific Ocean based on Hydroacoustic T-phases

Recorded by Cabled Seafloor Observatories. Apr. 2025. doi: 10.22541/au.174405179.94193080/v1.

Longuet-Higgins, M. A theory of the origin of microseisms. *Philosophical Transactions of the Royal Society of London. Series A, Mathematical and Physical Sciences*, 243(857):1–35, Sept. 1950. doi: 10.1098/rsta.1950.0012.

MacLeod, L. M. F. and Wilcock, W. S. D. Nonseismic Short-Duration Events Offshore Cascadia: Characteristics and Potential Origin. *Seismological Research Letters*, 96(2A):706–720, 02 2025. doi: 10.1785/0220240367.

Massel, S. R. *Ocean Surface Waves: Their Physics and Prediction*. WORLD SCIENTIFIC, Jan. 2013. doi: 10.1142/8682.

McCreery, C. S., Duennebier, F. K., and Sutton, G. H. Correlation of deep ocean noise (0.4–30 Hz) with wind, and the Holu Spectrum—A worldwide constant. *The Journal of the Acoustical Society of America*, 93(5):2639–2648, May 1993. doi: 10.1121/1.405838.

Meng, L., Huang, H., Bürgmann, R., Ampuero, J. P., and Strader, A. Dual megathrust slip behaviors of the 2014 Iquique earthquake sequence. *Earth and Planetary Science Letters*, 411:177–187, Feb. 2015. doi: 10.1016/j.epsl.2014.11.041.

Merle, S. G., Embley, R. W., Johnson, H. P., Lau, T.-K., Phrampus, B. J., Raineault, N. A., and Gee, L. J. Distribution of Methane Plumes on Cascadia Margin and Implications for the Landward Limit of Methane Hydrate Stability. *Frontiers in Earth Science*, 9, Mar. 2021. doi: 10.3389/feart.2021.531714.

Moore, J. C., Moore, G. F., Cochrane, G. R., and Tobin, H. J. Negative-polarity seismic reflections along faults of the Oregon accretionary prism: Indicators of overpressuring. *Journal of Geophysical Research: Solid Earth*, 100(B7):12895–12906, July 1995. doi: 10.1029/94jb02049.

Morton, E. A., Bilek, S. L., and Rowe, C. A. Newly detected earthquakes in the Cascadia subduction zone linked to seamount subduction and deformed upper plate. *Geology*, 46(11): 943–946, Sept. 2018. doi: 10.1130/g45354.1.

Morton, E. A., Bilek, S. L., and Rowe, C. A. Cascadia Subduction Zone Fault Heterogeneities From Newly Detected Small Magnitude Earthquakes. *Journal of Geophysical Research: Solid Earth*, 128(6), May 2023. doi: 10.1029/2023jb026607.

Nakano, M., Hori, T., Araki, E., Kodaira, S., and Ide, S. Shallow very-low-frequency earthquakes accompany slow slip events in the Nankai subduction zone. *Nature Communications*, 9(1), Mar. 2018. doi: 10.1038/s41467-018-03431-5.

NSF Ocean Observatories Initiative. Ocean Observatories Initiative, 2013. doi: 10.7914/SN/OO.

Obana, K. and Kodaira, S. Low-frequency tremors associated with reverse faults in a shallow accretionary prism. *Earth and Planetary Science Letters*, 287(1–2):168–174, Sept. 2009. doi: 10.1016/j.epsl.2009.08.005.

Obara, K. Nonvolcanic Deep Tremor Associated with Subduction in Southwest Japan. *Science*, 296(5573):1679–1681, May 2002. doi: 10.1126/science.1070378.

Ogiso, M. and Tamaribuchi, K. Spatiotemporal evolution of tremor activity near the Nankai Trough trench axis inferred from the spatial distribution of seismic amplitudes. *Earth, Planets and Space*, 74(1), Mar. 2022. doi: 10.1186/s40623-022-01601-w.

Okal, E. A. *The generation of T waves by earthquakes*, page 1–65. Elsevier, 2008. doi: 10.1016/s0065-2687(07)49001-x.

Peng, Z. and Gomberg, J. An integrated perspective of the continuum between earthquakes and slow-slip phenomena. *Nature Geoscience*, 3(9):599–607, Aug. 2010. doi: 10.1038/ngeo940.

Philip, B. T., Solomon, E. A., Kelley, D. S., Tréhu, A. M., Whorley, T. L., Roland, E., Tominaga, M., and Collier, R. W. Fluid sources and overpressures within the central Cascadia Subduction Zone revealed by a warm, high-flux seafloor seep. *Science Advances*, 9 (4), Jan. 2023. doi: 10.1126/sciadv.add6688.

Plata-Martinez, R., Ide, S., Shinohara, M., Garcia, E. S., Mizuno, N., Dominguez, L. A., Taira, T., Yamashita, Y., Toh, A., Yamada, T., Real, J., Husker, A., Cruz-Atienza, V. M., and Ito, Y. Shallow slow earthquakes to decipher future catastrophic earthquakes in the Guerrero seismic gap. *Nature Communications*, 12(1), June 2021. doi: 10.1038/s41467-021-24210-9.

Provost, F., Malet, J.-P., Hibert, C., Helmstetter, A., Radiguet, M., Amitrano, D., Langet, N., Larose, E., Abancó, C., Hürlimann, M., Lebourg, T., Levy, C., Le Roy, G., Ulrich, P., Vidal, M., and Vial, B. Towards a standard typology of endogenous landslide seismic sources. *Earth Surface Dynamics*, 6(4):1059–1088, Nov. 2018. doi: 10.5194/esurf-6-1059-2018.

Ragland, J., Schwock, F., Munson, M., and Abadi, S. An overview of ambient sound using Ocean Observatories Initiative hydrophones. *The Journal of the Acoustical Society of America*, 151 (3):2085–2100, Mar. 2022. doi: 10.1121/10.0009836.

Ramos, M. D., Huang, Y., Ulrich, T., Li, D., Gabriel, A., and Thomas, A. M. Assessing Margin-Wide Rupture Behaviors Along the Cascadia Megathrust With 3-D Dynamic Rupture Simulations. *Journal of Geophysical Research: Solid Earth*, 126(7), July 2021. doi: 10.1029/2021jb022005.

Remitti, F., Festa, A., Nirta, G., Barbero, E., and Mittempergher, S. Role of folding-related deformation in the seismicity of shallow accretionary prisms. *Nature Geoscience*, 17(7):600–607, June 2024. doi: 10.1038/s41561-024-01474-6.

Romanowicz, B., Stakes, D., Dolenc, D., Neuhauser, D., McGill, P., Uhrhammer, R., and Ramirez, T. The monterey bay broadband ocean bottom seismic observatory. *Annals of Geophysics*, 49 (2–3), Dec. 2006. doi: 10.4401/ag-3132.

Ross, D. and Kuperman, W. A. Mechanics of Underwater Noise. *The Journal of the Acoustical Society of America*, 86(4):1626–1626, Oct. 1989. doi: 10.1121/1.398685.

Rubinstein, J. L., Vidale, J. E., Gomberg, J., Bodin, P., Creager, K. C., and Malone, S. D. Non-volcanic tremor driven by large transient shear stresses. *Nature*, 448(7153):579–582, Aug. 2007. doi: 10.1038/nature06017.

Rubinstein, J. L., Gomberg, J., Vidale, J. E., Wech, A. G., Kao, H., Creager, K. C., and Rogers, G. Seismic wave triggering of nonvolcanic tremor, episodic tremor and slip, and earthquakes on Vancouver Island. *Journal of Geophysical Research: Solid Earth*, 114(B2), Feb. 2009a. doi: 10.1029/2008jb005875.

Rubinstein, J. L., Shelly, D. R., and Ellsworth, W. L. *Non-volcanic Tremor: A Window into the Roots of Fault Zones*, page 287–314. Springer Netherlands, 2009b. doi: 10.1007/978-90-481-2737-5_8.

Rudebusch, J. A., Prouty, N. G., Conrad, J. E., Watt, J. T., Kluesner, J. W., Hill, J. C., Miller, N. C., Watson, S. J., and Hillman, J. I. T. Diving deeper into seep distribution along the Cascadia convergent margin, United States. *Frontiers in Earth Science*, 11, Aug. 2023. doi: 10.3389/feart.2023.1205211.

Schmalzle, G. M., McCaffrey, R., and Creager, K. C. Central Cascadia subduction zone creep. *Geochemistry, Geophysics, Geosystems*, 15(4):1515–1532, Apr. 2014. doi: 10.1002/2013gc005172.

Schwartz, S. Y. and Rokosky, J. M. Slow slip events and seismic tremor at circum-Pacific subduction zones. *Reviews of Geophysics*, 45(3), Aug. 2007. doi: 10.1029/2006rg000208.

Schöpa, A., Chao, W.-A., Lipovsky, B. P., Hovius, N., White, R. S., Green, R. G., and Turowski, J. M. Dynamics of the Askja caldera July 2014 landslide, Iceland, from seismic signal analysis: precursor, motion and aftermath. *Earth Surface Dynamics*, 6(2): 467–485, June 2018. doi: 10.5194/esurf-6-467-2018.

Seydoux, L., Balestriero, R., Poli, P., Hoop, M. d., Campillo, M., and Baraniuk, R. Clustering earthquake signals and background noises in continuous seismic data with unsupervised deep learning. *Nature Communications*, 11(1), Aug. 2020. doi: 10.1038/s41467-020-17841-x.

Shelly, D. R., Beroza, G. C., and Ide, S. Non-volcanic tremor and low-frequency earthquake swarms. *Nature*, 446(7133):305–307, Mar. 2007. doi: 10.1038/nature05666.

Shen, Z. and Wu, W. Ocean bottom distributed acoustic sensing for T-wave detection and seismic ocean thermometry. Aug. 2023. doi: 10.22541/essoar.169186309.95288597/v1.

Sit, S., Brudzinski, M., and Kao, H. Detecting tectonic tremor through frequency scanning at a single station: Application to the Cascadia margin. *Earth and Planetary Science Letters*, 353–354:134–144, Nov. 2012. doi: 10.1016/j.epsl.2012.08.002.

Smith, L., Barth, J., Kelley, D., Plueddemann, A., Rodero, I., Ulses, G., Vardaro, M., and Weller, R. The Ocean Observatories Initiative. *Oceanography*, 31(1):16–35, Mar. 2018. doi: 10.5670/oceanog.2018.105.

Stone, I., Vidale, J. E., Han, S., and Roland, E. Catalog of Offshore Seismicity in Cascadia: Insights Into the Regional Distribution of Microseismicity and its Relation to Subduction Processes. *Journal of Geophysical Research: Solid Earth*, 123(1):641–652, Jan. 2018. doi: 10.1002/2017jb014966.

Sáez, M., Ruiz, S., Ide, S., and Sugioka, H. Shallow Nonvolcanic Tremor Activity and Potential Repeating Earthquakes in the Chile Triple Junction: Seismic Evidence of the Subduction of the Active Nazca–Antarctic Spreading Center. *Seismological Research Letters*, July 2019. doi: 10.1785/0220180394.

Takemura, S., Hamada, Y., Okuda, H., Okada, Y., Okubo, K., Akuhara, T., Noda, A., and Tonegawa, T. A review of shallow slow earthquakes along the Nankai Trough. *Earth, Planets and Space*, 75(1), Oct. 2023. doi: 10.1186/s40623-023-01920-6.

Talandier, J. and Okal, E. Identification Criteria for Sources of T Waves Recorded in French Polynesia. *Pure and Applied Geophysics*, 158(3):567–603, Mar. 2001. doi: 10.1007/pl00001195.

Tamaribuchi, K., Ogiso, M., and Noda, A. Spatiotemporal Distribution of Shallow Tremors Along the Nankai Trough, Southwest Japan, as Determined From Waveform Amplitudes and Cross-Correlations. *Journal of Geophysical Research: Solid Earth*, 127 (8), Aug. 2022. doi: 10.1029/2022jb024403.

Tary, J. B. Atypical Signals: Characteristics and Sources of Short-Duration Events, Dec. 2023. doi: 10.1002/9781119750925.ch8.

Tary, J. B., Géli, L., Guennou, C., Henry, P., Sultan, N., Çağatay, N., and Vidal, V. Microevents produced by gas migration and expulsion at the seabed: a study based on sea bottom recordings from the Sea of Marmara: Microevents produced by gas migration. *Geophysical Journal International*, 190(2):993–1007, June 2012. doi: 10.1111/j.1365-246x.2012.05533.x.

Todd, E. K., Schwartz, S. Y., Mochizuki, K., Wallace, L. M., Sheehan, A. F., Webb, S. C., Williams, C. A., Nakai, J., Yarce, J., Fry, B., Henrys, S., and Ito, Y. Earthquakes and Tremor Linked to Seamount Subduction During Shallow Slow Slip at the Hikurangi Margin, New Zealand. *Journal of Geophysical Research: Solid Earth*, 123 (8):6769–6783, Aug. 2018. doi: 10.1029/2018jb016136.

Toomey, D., Allen, R., Barclay, A., Bell, S., Bromirski, P., Carlson, R., Chen, X., Collins, J., Dziak, R., Evers, B., Forsyth, D., Gerstoft, P., Hooft, E., Livelybrooks, D., Lodewyk, J., Luther, D., McGuire, J., Schwartz, S., Tolstoy, M., Trehu, A., Weirathmueller, M., and Wilcock, W. The Cascadia Initiative: A Sea Change In Seismological Studies of Subduction Zones. *Oceanography*, 27(2):138–150, June 2014. doi: 10.5670/oceanog.2014.49.

Trowbridge, J., Weller, R., Kelley, D., Dever, E., Plueddemann, A., Barth, J. A., and Kawka, O. The Ocean Observatories Initiative. *Frontiers in Marine Science*, 6, Mar. 2019. doi: 10.3389/fmars.2019.00074.

Tréhu, A. A note on the effect of bottom currents on an ocean bottom seismometer. *Bulletin of the Seismological Society of America*, 75(4):1195–1204, 08 1985. doi: 10.1785/BSSA0750041195.

Tréhu, A. M., Blakely, R. J., and Williams, M. C. Subducted seamounts and recent earthquakes beneath the central Cascadia forearc. *Geology*, 40(2):103–106, Feb. 2012. doi: 10.1130/g32460.1.

Tréhu, A. M., Braunmiller, J., and Davis, E. Seismicity of the Central Cascadia Continental Margin near 44.5 N: A Decadal View. *Seismological Research Letters*, 86(3):819–829, Apr. 2015. doi: 10.1785/0220140207.

Tréhu, A. M., de Moor, A., Madrid, J. M., Sáez, M., Chadwell, C. D., Ortega-Culaciati, F., Ruiz, J., Ruiz, S., and Tryon, M. D. Postseismic response of the outer accretionary prism after the 2010 Maule earthquake, Chile. *Geosphere*, 16(1):13–32, Dec. 2019. doi: 10.1130/ges02102.1.

Tsang-Hin-Sun, E., Batsi, E., Klingelhoefer, F., and Géli, L. Spatial and temporal dynamics of gas-related processes in the Sea of Marmara monitored with ocean bottom seismometers. *Geophysical Journal International*, 216(3):1989–2003, Dec. 2018. doi: 10.1093/gji/ggy535.

Vouillamoz, N., Rothmund, S., and Joswig, M. Characterizing the complexity of microseismic signals at slow-moving clay-rich debris slides: the Super-Sauze (southeastern France) and Pechgraben (Upper Austria) case studies. *Earth Surface Dynamics*, 6(2):525–550, June 2018. doi: 10.5194/esurf-6-525-2018.

Wagstaff, R. An Ambient Noise Model for the Northeast Pacific Ocean Basin. *IEEE Journal of Oceanic Engineering*, 30(2): 286–294, Apr. 2005. doi: 10.1109/joe.2004.836993.

Walker, D., McCreery, C., and Hiyoshi, Y. T-phase spectra, seismic moments, and tsunamigenesis. *Bulletin of the Seismological Society of America*, 82(3):1275–1305, 1992. doi: 10.1785/BSSA0820031275.

Wallace, L., Sheehan, A., Schwartz, S., and Webb, S. Hikurangi Ocean Bottom Investigation of Tremor and Slow Slip, 2014. doi: 10.7914/SN/YH$_2$014.

Wallace, L. M., Webb, S. C., Ito, Y., Mochizuki, K., Hino, R., Henrys, S., Schwartz, S. Y., and Sheehan, A. F. Slow slip near the trench at the Hikurangi subduction zone, New Zealand. *Science*, 352 (6286):701–704, May 2016. doi: 10.1126/science.aaf2349.

Walter, J. I., Schwartz, S. Y., Protti, J. M., and Gonzalez, V. Persistent tremor within the northern Costa Rica seismogenic zone. *Geophysical Research Letters*, 38(1), Jan. 2011. doi: 10.1029/2010gl045586.

Walter, J. I., Schwartz, S. Y., Protti, M., and Gonzalez, V. The synchronous occurrence of shallow tremor and very low frequency earthquakes offshore of the Nicoya Peninsula, Costa Rica. *Geophysical Research Letters*, 40(8):1517–1522, Apr. 2013. doi: 10.1002/grl.50213.

Webb, S. C. Broadband seismology and noise under the ocean. *Reviews of Geophysics*, 36(1):105–142, Feb. 1998. doi: 10.1029/97rg02287.

Wech, A. G. Interactive Tremor Monitoring. *Seismological Research Letters*, 81(4):664–669, July 2010. doi: 10.1785/gssrl.81.4.664.

Wech, A. G. Cataloging Tectonic Tremor Energy Radiation in the Cascadia Subduction Zone. *Journal of Geophysical Research: Solid Earth*, 126(10), Oct. 2021. doi: 10.1029/2021jb022523.

Wech, A. G. and Creager, K. C. Automated detection and location of Cascadia tremor. *Geophysical Research Letters*, 35(20), Oct. 2008. doi: 10.1029/2008gl035458.

Wech, A. G., Sheehan, A. F., Boese, C. M., Townend, J., Stern, T. A.,

and Collins, J. A. Tectonic Tremor Recorded by Ocean Bottom Seismometers. *Seismological Research Letters*, 84(5):752–758, Sept. 2013. doi: 10.1785/0220120184.

Welch, P. The use of fast Fourier transform for the estimation of power spectra: A method based on time averaging over short, modified periodograms. *IEEE Transactions on Audio and Electroacoustics*, 15(2):70–73, June 1967. doi: 10.1109/tau.1967.1161901.

Wilcock, W. S., Stafford, K. M., Andrew, R. K., and Odom, R. I. Sounds in the Ocean at 1–100 Hz. *Annual Review of Marine Science*, 6(1):117–140, Jan. 2014. doi: 10.1146/annurev-marine-121211-172423.

Williams, M. C., Trehu, A. M., and Braunmiller, J. Seismicity at the Cascadia Plate Boundary beneath the Oregon Continental Shelf. *Bulletin of the Seismological Society of America*, 101(3):940–950, May 2011. doi: 10.1785/0120100198.

Woods, K., Wallace, L. M., Williams, C. A., Hamling, I. J., Webb, S. C., Ito, Y., Palmer, N., Hino, R., Suzuki, S., Savage, M. K., Warren-Smith, E., and Mochizuki, K. Spatiotemporal Evolution of Slow Slip Events at the Offshore Hikurangi Subduction Zone in 2019 Using GNSS, InSAR, and Seafloor Geodetic Data. *Journal of Geophysical Research: Solid Earth*, 129(8), Aug. 2024. doi: 10.1029/2024jb029068.

Yamashita, Y., Yakiwara, H., Asano, Y., Shimizu, H., Uchida, K., Hirano, S., Umakoshi, K., Miyamachi, H., Nakamoto, M., Fukui, M., Kamizono, M., Kanehara, H., Yamada, T., Shinohara, M., and Obara, K. Migrating tremor off southern Kyushu as evidence for slow slip of a shallow subduction interface. *Science*, 348(6235): 676–679, May 2015. doi: 10.1126/science.aaa4242.

Yokota, Y., Ishikawa, T., Watanabe, S.-i., Tashiro, T., and Asada, A. Seafloor geodetic constraints on interplate coupling of the Nankai Trough megathrust zone. *Nature*, 534(7607):374–377, May 2016. doi: 10.1038/nature17632.